Molecular Therapy
Original Article

Cyclase-associated protein 2 gene delivery: A potential multi-target approach for preventing synaptic failure in Alzheimer's disease

Ramona Stringhi,[1,5] Silvia Pelucchi,[1,5] Laura D'Andrea,[1] Filippo La Greca,[1] Elisa Zianni,[1] Lorenzo Targa,[1] Cedric Mosconi,[1] Lina Vandermeulen,[1] Miriam Ascagni,[2] Michela Carola Speciani,[3] Fabrizio Gardoni,[1] Diego Scheggia,[1] Valeria Edefonti,[3,4] Monica Di Luca,[1] and Elena Marcello[1]

[1]Department of Pharmacological and Biomolecular Sciences "Rodolfo Paoletti," Università degli Studi di Milano, Via Giuseppe Balzaretti 9, 20133 Milan, Italy; [2]Unitech NOLIMITS, Università degli Studi di Milano, Via Golgi 19, 20133 Milan, Italy; [3]Department of Clinical Sciences and Community Health – Dipartimento di Eccellenza 2023-2027, Branch of Medical Statistics, Biometry and Epidemiology "G. A. Maccacaro," Università degli Studi di Milano, Via Celoria 22, 20133 Milan, Italy; [4]Fondazione IRCCS Ca' Granda Ospedale Maggiore Policlinico, Via Sforza 35, 20122 Milan, Italy

Alzheimer's disease (AD) is marked by synaptic failure, with actin cytoskeleton alterations playing a key role in its pathogenesis. Cofilin, a regulator of actin dynamics in dendritic spines, forms cofilin-actin rods upon exposure to amyloid-β (Aβ) oligomers, contributing to synaptic loss. Cyclase-associated protein 2 (CAP2) is crucial for regulating cofilin activity. During long-term potentiation, CAP2 dimerization is relevant for cofilin translocation to spines required for spine remodeling. In AD, CAP2 is downregulated, thus disrupting synaptic CAP2/cofilin complexes. To investigate the neuroprotective potential of CAP2 overexpression in preventing Aβ-induced synaptic dysfunction, we used adeno-associated virus serotype 9 (AAV) gene delivery to elevate CAP2 levels in APP/PS1 mice—a model of amyloid pathology—starting from the asymptomatic stage. APP/PS1 animals received bilateral stereotaxic injection of either AAV expressing CAP2 or a control AAV. This approach preserved synaptic CAP2/cofilin interaction, maintained synaptic plasticity pathways, and sustained cognitive function. CAP2 overexpression reduced cofilin-actin rod formation and mitigated tau abnormalities. Notably, CAP2 is present in cofilin-actin rods, and its dimerization is required to prevent Aβ-driven synaptic loss but not to protect neurons from rod formation. These findings highlight CAP2 upregulation as a promising strategy to enhance neuronal resilience and counteract Aβ synaptic toxicity in AD.

INTRODUCTION

The actin cytoskeleton plays a pivotal role in supporting neuronal structure and function. Actin dynamics drive structural changes that can modify synaptic function in mature synapses, which are capable of activity-dependent remodeling in response to changed input and activity patterns.[1]

Given the substantial contribution of the cytoskeleton to mechanisms involved in synaptic plasticity, an impairment in actin dynamics can contribute to neurodegenerative disorders such as Alzheimer's disease (AD), in which plasticity events are disrupted from the early stages of the disease.[2] Indeed, alterations of the actin cytoskeletal network have been found in neuronal cells of AD patients alongside hallmark pathogenic events such as the aggregation of amyloid-β (Aβ) plaques, formation of neurofibrillary tangles, and synaptic loss. In particular, the presence of cytoplasmic rod-like inclusions of ADP-actin and active dephosphorylated cofilin in a 1:1 ratio has been reported in the brains of AD patients and mouse models.[3] The formation of rod-shaped bundles can be triggered by a variety of stress-responsive cell signaling pathways,[4] including those induced by exposure to Aβ.[5,6] Cofilin-actin rods interfere with physiological cytoskeletal dynamics and sequester cofilin from the synaptic compartment, where it is required for activity-dependent spine remodeling. Thus, the presence of cofilin-actin rods has been proposed to be implicated in Aβ-induced synaptic loss.[4,7,8]

In dendritic spines, cofilin transiently severs filaments, creating free ends that polymerize and branch to increase the size and complexity of the actin cytoskeleton.[9] Cofilin activity therefore plays a major role in promoting F-actin assembly and spine growth.[10–12] The cofilin activity that promotes F-actin dynamics is enhanced by different proteins including cyclase-associated proteins (CAPs).[13] CAPs are modular proteins that assemble into tetramers and hexamers,[14,15] facilitating actin filament turnover through distinct mechanisms.[16–18] In mammals, there are two CAP genes: CAP1 is ubiquitously expressed, while CAP2 is expressed primarily in neurons, muscle, and skin.[19] We have previously described a neuronal

Received 28 March 2025; accepted 8 December 2025;
https://doi.org/10.1016/j.ymthe.2025.12.023.

[5]These authors contributed equally

Correspondence: Elena Marcello, Department of Pharmacological and Biomolecular Sciences "Rodolfo Paoletti," Università degli Studi di Milano, Via Giuseppe Balzaretti 9, Milan 20133, Italy.
E-mail: elena.marcello@unimi.it

Please cite this article in press as: Stringhi et al., Cyclase-associated protein 2 gene delivery: A potential multi-target approach for preventing synaptic failure in Alzheimer's disease, Molecular Therapy (2025), https://doi.org/10.1016/j.ymthe.2025.12.023

mechanism, through which the dimerization of CAP2, dependent on Cys^{32}, plays a crucial role in actin dynamics. CAP2 dimerization is essential for targeting cofilin to spines upon long-term potentiation (LTP) induction, thereby promoting spine remodeling and the enhancement of synaptic transmission.[20] This plasticity-regulated mechanism is altered in the hippocampus of AD patients and relevant animal models.[20] CAP2 expression is reduced in AD, meaning lower synaptic availability of the CAP2 dimer. In the AD hippocampus, cofilin exhibits altered association with CAP2 dimer and aberrant spine localization.[20] In addition, our recent study demonstrates that altered CAP2 levels in cerebrospinal fluid (CSF) are detectable from the prodromal stage of AD and correlate with tau-related pathological changes.[21]

Considering the involvement of cofilin and its protein partners in multiple pathological traits of AD, this actin-binding protein can be considered a "master node" in AD pathogenesis[3] and could serve as a potential target to preserve neuronal function.

In this study, we developed a strategy to prevent abnormal compartmentalization of cofilin in AD neurons by enhancing the expression of its partner CAP2. We intended to test the concept that increasing CAP2 levels through a gene delivery approach can represent an innovative strategy for preventing AD synaptic failure. To this end, we used direct overexpression of CAP2 by AAV-mediated gene transfer into the hippocampus to explore its potential to delay the onset of cognitive deficits in APP/PS1 mice, a model of amyloid pathology suitable for assessing the neuroprotective potential of CAP2 in preventing Aβ-dependent synaptic dysfunction.[22]

Our findings demonstrate that the early-stage overexpression of CAP2 in the hippocampus of APP/PS1 mice effectively prevented the onset of cognitive deficits. This intervention preserved functional CAP2/cofilin complexes at the synapse and reduced the formation of actin rods and cytoskeletal abnormalities, without influencing plaque deposition. Taking advantage of an *in vitro* system, we found that CAP2 is a component of mature cofilin-actin rods specifically induced by Aβ oligomers. The CAP2/cofilin complex is an early target of Aβ oligomers, which affect CAP2 dimerization and its association with cofilin. Finally, we found that CAP2 dimerization is essential to prevent Aβ-induced dendritic spine loss, but not for protection from cofilin-actin rod formation.

RESULTS

CAP2 overexpression in the hippocampus of a mouse model of amyloid pathology prevents the alterations of the CAP2/cofilin complex at the synapse

CAP2 protein levels are selectively reduced in the hippocampus of AD patients, whereas no changes are detected in the superior frontal gyrus.[20] To strengthen these data, we measured CAP2 mRNA levels in postmortem specimens obtained from sporadic AD patients, fulfilling criteria for Braak stages 4 and 5, and age-matched control subjects (HCs) (Table S1). The RT-qPCR results revealed a significant decrease in *CAP2* mRNA levels in the hippocampus of AD patients compared with HCs (Figure S1A), indicating a reduced expression of the *CAP2* gene in AD. Supporting these results, a recent large-scale proteomic analysis of AD patients led to the development of NeuroPro, a comprehensive database that enables meta-analysis of disease-associated protein changes.[23] Analysis using this database has validated the downregulation of CAP2 in AD hippocampus.

Given these findings, we investigated the neuroprotective potential of CAP2 in preventing amyloid-induced synaptic failure. To this end, we used the APP/PS1 mouse model, previously characterized by our group for CAP2 dysregulation.[20] We delivered CAP2 to the hippocampus of 4-month-old APP/PS1 mice via AAV-mediated overexpression, targeting the asymptomatic phase prior to the onset of cognitive deficits, which typically emerge around 6 months of age (Figures S1B and S1C).[22,24] Notably, CAP2 downregulation has been reported in APP/PS1 mice at the age of 6 months,[20] while its expression and synaptic localization remain unchanged at 4 months when compared with wild-type (WT) animals (Figure S1D).

We employed an AAV-based bicistronic vector coding for eGFP and myc-tagged murine CAP2 (AAV9-hSyn-eGFP:T2A:mycCAP2, referred to as AAV-mycCAP2). The mycCAP2 reading frame was fused to eGFP by a T2A site to enable tracking of transduced cells. Expression was driven by the neuronal synapsin promoter (Figure 1A). We selected AAV serotype 9 due to its high efficiency in mediating transgene expression in the hippocampus and its strong neuronal tropism.[25] To determine the optimal dose of AAV for hippocampal delivery, we performed a pilot experiment in WT mice. Two different doses (4×10^{10} and 8×10^{10} genome copies, GCs) of the AAV were unilaterally injected into one hippocampus, with the contralateral side serving as an internal control. Mice were euthanized 4 weeks post-injection (Figure S2A), and western blot (WB) analysis revealed that the lower dose was sufficient to induce an increase in CAP2 protein levels in the hippocampus (Figure S2B).

To assess the effect of CAP2 overexpression on the progression of amyloid-dependent synaptic dysfunction, adult APP/PS1 mice received bilateral stereotaxic injections at 4 months of age with either AAV-mycCAP2 or a monocistronic control vector (AAV9-hSyn-eGFP, hereafter referred to as AAV-GFP) (Figure 1B).

To evaluate CAP2 and GFP expression, animals were euthanized 8 weeks post-injection and brain samples were analyzed by WB and immunohistochemistry (IHC) using myc-tag-, GFP-, and CAP2-specific antibodies. Analysis of coronal brain sections revealed widespread expression of CAP2 in the hippocampus, without spreading in other brain regions (Figures S2C and S2D). WB analysis of hippocampal homogenates confirmed efficient AAV-mediated CAP2 expression in injected animals (Figure S2E).

To investigate the effect of CAP2 overexpression on the regulation of cofilin availability at the synapse, we took advantage of a biochemical fractionation approach to purify the Triton-insoluble fraction (TIF), which is enriched in postsynaptic proteins, from the hippocampus of

Please cite this article in press as: Stringhi et al., Cyclase-associated protein 2 gene delivery: A potential multi-target approach for preventing synaptic failure in Alzheimer's disease, Molecular Therapy (2025), https://doi.org/10.1016/j.ymthe.2025.12.023

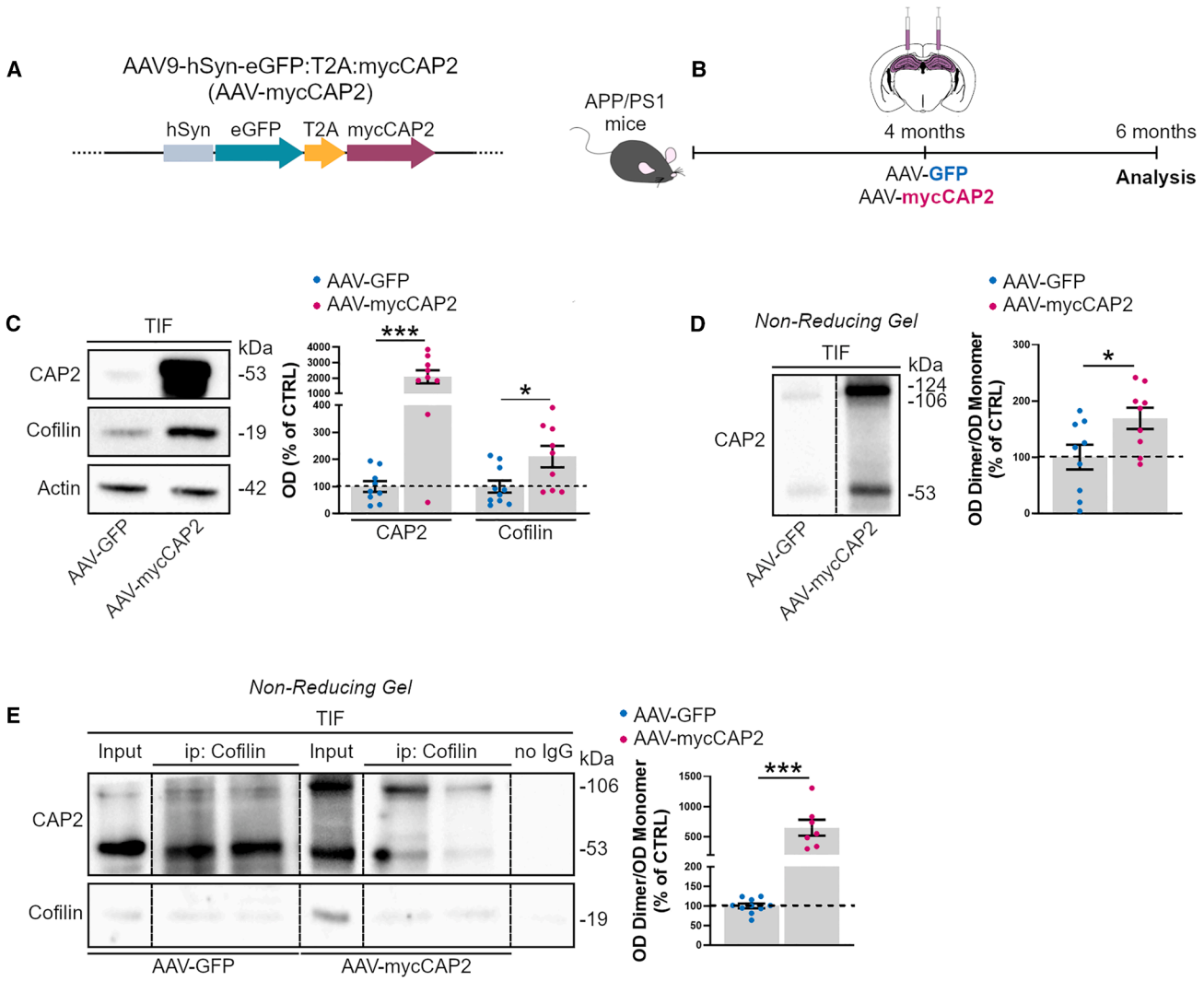

Figure 1. Increasing CAP2 levels in APP/PS1 mice hippocampus preserves CAP2 dimer-cofilin synaptic pathway

(A) Schematic representation of the AAV expression vector used for stereotaxic injection. The construct includes the human synapsin I promoter (hSyn) for neuron-specific expression, followed by eGFP as a fluorescent reporter. A T2A self-cleaving peptide enables co-expression of the reporter with the myc-tagged CAP2 protein (mycCAP2) from a single transcript. (B) Experimental paradigm: 4-month-old APP/PS1 mice were bilaterally stereotaxically injected with the viral vector AAV9-hSyn-eGFP:T2A:mycCAP2 (AAV-mycCAP2) to overexpress CAP2 in the whole hippocampus. As a control, the vector AAV9-hSyn-eGFP (AAV-GFP) was used. At the age of 6 months the biochemical analysis was carried out. (C) Representative WB showing the expression of CAP2, cofilin, and actin in hippocampal Triton-insoluble fraction (TIF) samples of 6-month-old APP/PS1 mice injected with AAV-mycCAP2 compared with GFP-injected animals. The quantification of optical density (OD) and its normalization to the loading control OD (actin) shows that both CAP2 and cofilin synaptic levels are increased in CAP2-injected mice (CAP2, AAV-GFP = 100 ± 20.02, AAV-mycCAP2 = 2083 ± 423.8, cofilin, AAV-GFP = 100 ± 22.08, AAV-mycCAP2 = 210.4 ± 39.43; two-tailed unpaired *t* test: ***$p = 0.0003$, *$p = 0.0225$, $n = 9$–10 mice). (D) Representative WB of CAP2 dimer levels in hippocampal TIF samples of CAP2- and GFP-injected mice. Samples were loaded onto a non-reducing SDS-PAGE to detect a band corresponding to the CAP2 monomer, representing denatured CAP2 forms migrating at the expected molecular weight in SDS-PAGE, along with a 106 kDa band corresponding to the dimeric form. In CAP2-injected mice, a further band at 124 kDa, corresponding to mycCAP2 dimer, was revealed. To perform quantitative analysis, CAP2 dimer levels were normalized to CAP2 monomer (expressed as CAP2 dimer/monomer ratio), which served as our standardized measurement throughout all subsequent analyses. Statistical analysis highlights an augmented CAP2 dimer/monomer ratio in mice injected with AAV-mycCAP2 compared with controls (CAP2, AAV-GFP = 100 ± 21.91, AAV-mycCAP2 = 169 ± 18.85; two-tailed unpaired *t* test: *$p = 0.0296$, $n = 9$ mice). Dashed lines indicate that the images come from different parts of the same gel. (E) TIF samples obtained from the hippocampus of CAP2- or GFP-injected APP/PS1 mice were immunoprecipitated (ip) with anti-cofilin antibody. The coprecipitation of CAP2 was evaluated by loading the samples in a non-denaturating condition. The results highlight that cofilin binding to CAP2 dimer is increased in the TIF fraction of CAP2-overexpressing mice compared with GFP controls (CAP2 dimer/monomer, AAV-GFP = 100 ± 5.898, AAV-mycCAP2 = 650.7 ± 131.6; two-tailed unpaired *t* test: ***$p = 0.0001$, $n = 7$–10 mice). Dashed lines indicate that the images come from different parts of the same gel or from different gels. All data are presented as the percentage of control AAV-GFP-injected mice and expressed as mean ± SE. IgG, immunoglobulin.

Please cite this article in press as: Stringhi et al., Cyclase-associated protein 2 gene delivery: A potential multi-target approach for preventing synaptic failure in Alzheimer's disease, Molecular Therapy (2025), https://doi.org/10.1016/j.ymthe.2025.12.023

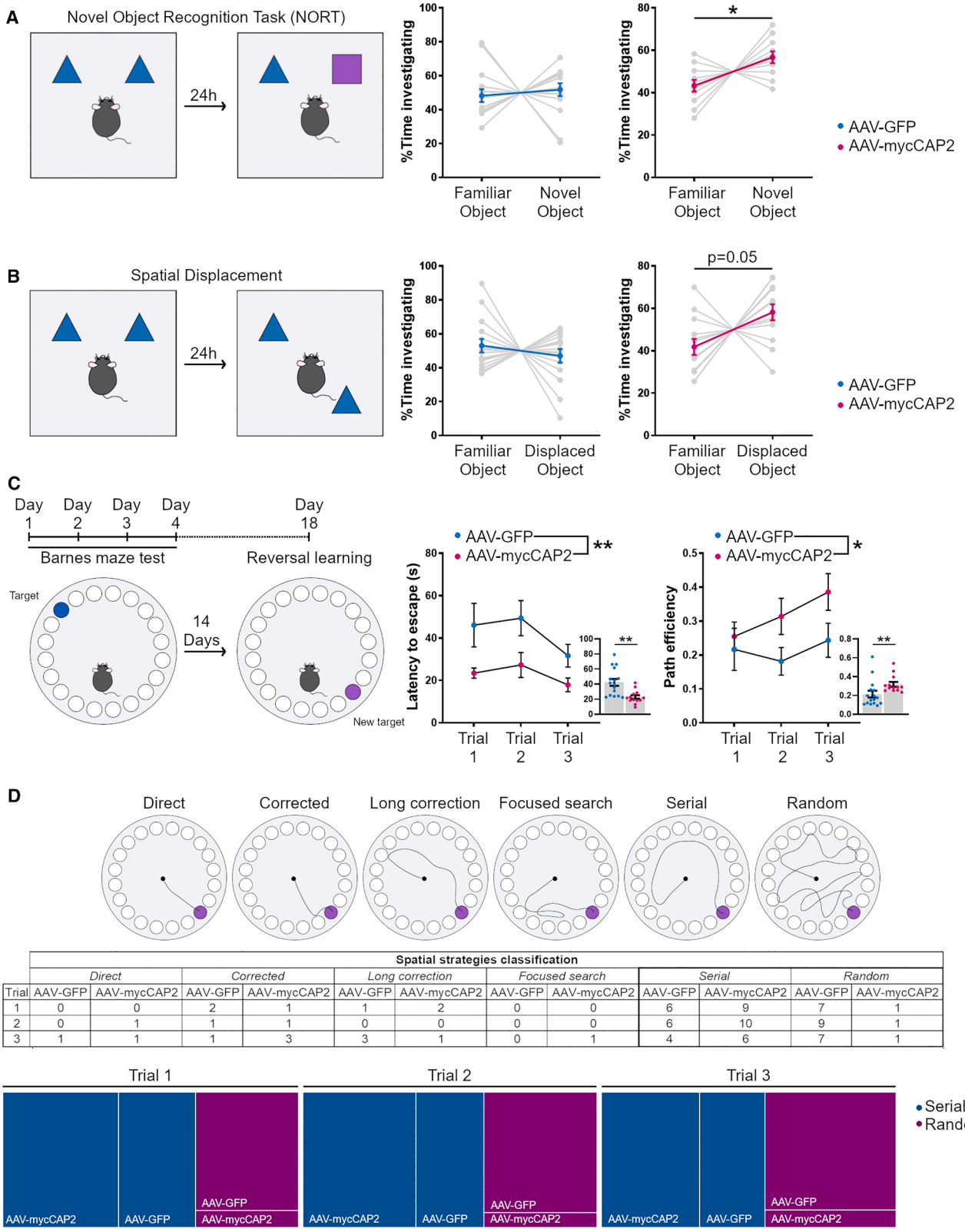

Spatial strategies classification												
	Direct		*Corrected*		*Long correction*		*Focused search*		*Serial*		*Random*	
Trial	AAV-GFP	AAV-mycCAP2	AAV-GFP	AAV-mycCAP2	AAV-GFP	AAV-mycCAP2	AAV-GFP	AAV-mycCAP2	AAV-GFP	AAV-mycCAP2	AAV-GFP	AAV-mycCAP2
1	0	0	2	1	1	2	0	0	6	9	7	1
2	0	1	1	1	0	0	0	0	6	10	9	1
3	1	1	1	3	3	1	0	1	4	6	7	1

(legend on next page)

both CAP2- and GFP-injected APP/PS1 mice (Figure 1B). As expected, WB analyses of hippocampal homogenates revealed a significant increase in total CAP2 levels in CAP2-injected APP/PS1 mice compared with GFP-injected animals (Figure S2F). No difference in the total abundance of cofilin between groups was detected (Figure S2F). The increase in CAP2 expression led to a significant augmentation of both CAP2 and cofilin postsynaptic levels in CAP2-injected APP/PS1 mice compared with the control group (Figure 1C).

CAP2 exhibits oligomerization properties, existing in multiple molecular forms through self-association. LTP triggers Cys^{32}-dependent CAP2 homodimerization and the association of the CAP2 homodimer to cofilin.[20] The reduced association between cofilin and Cys^{32}-dependent CAP2 dimers in the AD hippocampus suggests impaired CAP2/cofilin complex formation at hippocampal synapses.[20] Therefore, we tested the effect of CAP2 overexpression on the CAP2 dimer levels and the association of CAP2 forms to cofilin. To detect levels of CAP2 dimer, the samples were loaded onto a non-reducing SDS-PAGE. WB analysis revealed a significant increase in the CAP2 dimer in both the total homogenate (Figure S2G) and in the postsynaptic fraction (TIF) of CAP2-injected APP/PS1 mice when compared with the control group (Figure 1D). To check the association with cofilin, samples of the hippocampal postsynaptic fraction (TIF) were immunoprecipitated using an antibody against cofilin and loaded onto a non-reducing gel. WB analysis carried out with a CAP2 antibody showed that in the postsynaptic compartment, the CAP2 dimer associated with cofilin was significantly increased when CAP2 was overexpressed (Figure 1E).

These results suggest that increasing CAP2 levels promotes CAP2 dimerization and the association of the CAP2 homodimer to cofilin and subsequently increases the synaptic availability of cofilin.

CAP2 overexpression in the hippocampus of APP/PS1 mice prevents cognitive deficits

To assess the effect of CAP2 overexpression on cognitive function and memory formation, we used the same experimental paradigm (Figure 1B) to test CAP2- or GFP-injected APP/PS1 mice in the novel object recognition task (NORT). Mice were presented with two identical objects and following a 24-h delay, one of these was replaced with a novel one (Figure 2A). As expected, GFP-injected APP/PS1 mice did not discriminate between the familiar and the novel object, confirming their cognitive impairment. On the other hand, CAP2-injected APP/PS1 mice showed a clear preference for the novel over the familiar object, indicating that CAP2 overexpression prevented cognitive impairments in APP/PS1 mice.

To assess hippocampal-dependent memory, we performed a spatial displacement task. Mice were placed in an open field arena in the presence of two identical objects and after a 24-h delay, one of the two objects was relocated (Figure 2B). GFP-injected APP/PS1 mice did not show any object preference, whereas the CAP2 group spent more time exploring the displaced object, indicating that these mice could make a distinction between the two objects based on spatial information. We did not observe differences between the two groups in locomotor activity (total travel distance, Figure S3A) or anxiety-like behavior (time freezing, time in the center, Figures S3B and S3C) in either task conducted in the open field arena, indicating that the manipulation of CAP2 expression had a specific effect on cognitive behavior. Taken together, these results suggest that increasing CAP2 levels in the hippocampus of AD mice could prevent cognitive deficits at early stages.

To address hippocampal-dependent spatial learning and memory in more detail, we tested CAP2- and GFP-injected APP/PS1 mice in the Barnes maze, in which mice learn to identify a specific target area (escape box) using external visual cues. Mice were trained to find the target area across three daily trials over 4 days (Figure 2C). However, we did not find any difference in the time to identify the target area (latency to escape) between CAP2- and GFP-injected APP/PS1 mice (Figure S3D). Two weeks after initial task acquisition, we assessed the reversal learning ability of CAP2- and GFP-injected APP/PS1 mice by testing a single daily session of three trials in the same maze, with the target area displaced by 180° (Figure 2C). In this condition, CAP2-injected APP/PS1 mice showed a reduced latency to escape compared with GFP-injected APP/PS1 mice (Figure 2C). We also quantified the difference in choice strategy by computing a path efficiency score, where higher values indicate the choice of more efficient strategies to reach the target area. We found that CAP2-injected APP/PS1 mice showed higher scores across trials compared with GFP-injected APP/PS1 mice (Figure 2C).

Figure 2. CAP2 overexpression in 6-month-old APP/PS1 mice hippocampus prevents cognitive defects

(A) Schematic of the NORT. Preference was calculated as the exploration time ratio of the familiar (or novel) object to total exploration time. GFP mice indiscriminately explored familiar and novel objects, while CAP2 mice spent more time investigating the novel object (AAV-GFP, familiar object = 48.23 ± 3.779, novel object = 51.77 ± 3.779, AAV-mycCAP2, familiar object = 43.31 ± 2.766, novel object = 56.69 ± 2.766; two-tailed paired *t* test: $^{*}p = 0.0361$, $n = 11$–15 mice). (B) Diagram of the spatial displacement test. CAP2-injected mice showed a preference for the displaced object, unlike the GFP controls (AAV-GFP, familiar object = 53.03 ± 3.979, displaced object = 46.97 ± 3.979, AAV-mycCAP2, familiar object = 41.85 ± 3.765, displaced object = 58.15 ± 3.765; two-tailed paired *t* test: $p = 0.05$, $n = 13$–15 mice). (C) Overview of the Barnes maze and reversal learning test. The results of the reversal learning task highlight a significant difference between the GFP and CAP2 groups in the latency to escape. The inset shows that the average time, along the three trials, was higher in GFP-injected mice. The graphs on the right show that CAP2-injected mice adopt a more efficient search pattern (Latency to escape, two-way RM ANOVA: $^{**}p = 0.0014$, $n = 13$–16 mice; inset, AAV-GFP = 42.37 ± 4.499, AAV-mycCAP2 = 22.87 ± 2.447, two-tailed unpaired *t* test: $^{**}p = 0.0014$, $n = 13$–16 mice; Path efficiency, two-way RM ANOVA: $^{*}p = 0.0296$, $n = 13$–16 mice; inset, AAV-GFP = 0.2137 ± 0.03537, AAV-mycCAP2 = 0.3181 ± 0.02531, Mann-Whitney test: $^{**}p = 0.0048$, $n = 13$–16 mice). (D) Example diagrams illustrating different search strategies analyzed. The table reports the number of CAP2 or GFP mice that used the different search strategies in the three trials. The graphs represent the percentage of CAP2 or GFP mice employing random (violet) and serial (blue) search strategies across the three trials of the reversal learning task. CAP2-injected mice utilized the serial search strategy more frequently than the control group.

Please cite this article in press as: Stringhi et al., Cyclase-associated protein 2 gene delivery: A potential multi-target approach for preventing synaptic failure in Alzheimer's disease, Molecular Therapy (2025), https://doi.org/10.1016/j.ymthe.2025.12.023

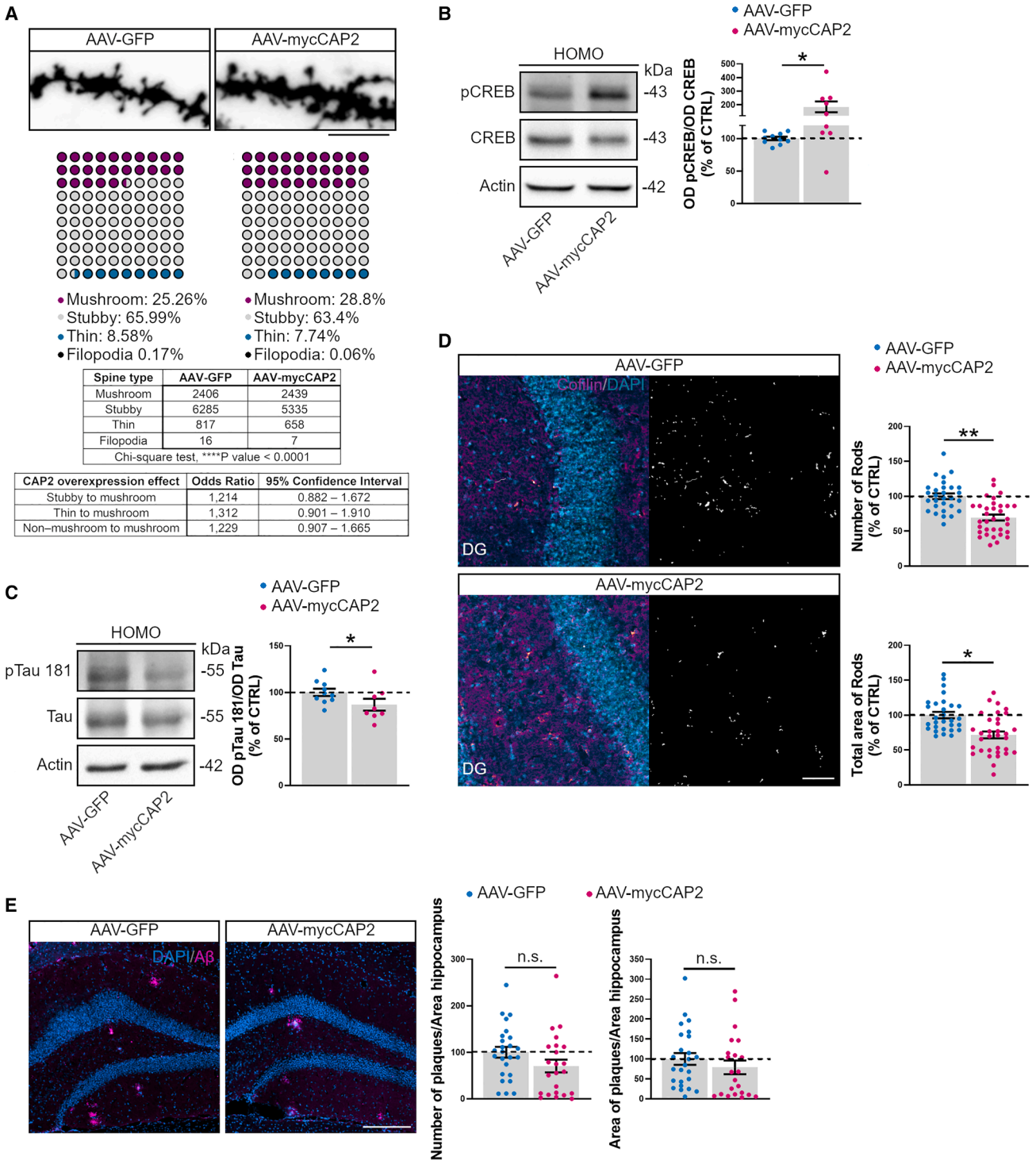

Spine type	AAV-GFP	AAV-mycCAP2
Mushroom	2406	2439
Stubby	6285	5335
Thin	817	658
Filopodia	16	7
Chi-square test, ****P value < 0.0001		

CAP2 overexpression effect	Odds Ratio	95% Confidence Interval
Stubby to mushroom	1,214	0.882 – 1.672
Thin to mushroom	1,312	0.901 – 1.910
Non–mushroom to mushroom	1,229	0.907 – 1.665

Figure 3. Enhancing CAP2 levels in APP/PS1 mice hippocampus maintains synaptic plasticity-related pathways and prevents cytoskeleton defects, without affecting plaque load

(A) Representative confocal images of hippocampal dendritic spines of APP/PS1 mice receiving AAV-mycCAP2 or AAV-GFP injection. Scale bar, 5 μm. The joint distribution of dendritic spine type and treatment is reported in the table together with the *p* value of the chi-square test of independence (AAV-GFP $n = 9{,}524$ spines, AAV-mycCAP2 $n = 8{,}439$ spines, $p < 0.0001$). (B) Representative WB showing the expressions of pCREB, CREB, and actin, as the loading control, in hippocampal homogenate samples of

(legend continued on next page)

Please cite this article in press as: Stringhi et al., Cyclase-associated protein 2 gene delivery: A potential multi-target approach for preventing synaptic failure in Alzheimer's disease, Molecular Therapy (2025), https://doi.org/10.1016/j.ymthe.2025.12.023

To better understand how mice used spatial information during the reversal learning session, we analyzed the search strategies used to identify the target areas. Based on their trajectories, we automatically classified the search patterns into six distinct categories: direct, corrected, long correction, focused search, serial, and random (Figure 2D). To quantify potential treatment effects on strategy choice, we applied a generalized linear mixed-effects model (GLMM) with a logit link and binomial distribution. In this analysis, treatment with CAP2 significantly influenced strategy selection (β: 3.936, SE: 1.575, p value: 0.013, reference category: GFP). In contrast, the trial number had no significant effect (trial #2: β: −0.08906, SE: 0.89169, p value: 0.920; trial #3: β: −0.506, SE: 0.951, p value: 0.594, reference category: trial #1), and we found no significant interaction between treatment and trial number; the standard deviation of the random-effect term for mouse ID was equal to 1.883. Importantly, the odds ratio analysis revealed that mice treated with CAP2 were about 50 times more likely to switch from a random to a serial search strategy compared with GFP controls (odds ratio = 51.2; 95% CI: 2.3–1,122.5). This suggests that CAP2 treatment strongly promoted more structured and efficient search strategies during the reversal learning phase.

To evaluate the long-term effects of the treatment, we tested mice at 9 months of age using the Barnes maze (Figure S3E). Notably, AAV expression remained localized in the hippocampus (Figure S3F). Consistent with the results observed in 6-month-old mice, the path efficiency scores confirmed that CAP2-overexpressing mice outperformed GFP-injected controls. Specifically, these mice demonstrated significantly higher path efficiency scores (Figure S3G), indicating their ability to adopt more effective strategies to reach the target area. These results suggest that CAP2 overexpression ameliorates cognitive function in APP/PS1 mice when acquired information is applied under novel circumstances.

CAP2 overexpression promotes synaptic plasticity-related pathways and ameliorates cytoskeleton abnormalities in APP/PS1 mice

Having established that AAV-CAP2 expression ameliorated the cognitive deficits of APP/PS1 mice, we evaluated whether the effects on cognitive performance were accompanied by changes in spine morphology and signaling pathways associated with synaptic plasticity phenomena in the hippocampus of treated mice.

We analyzed spine shape using carbocyanine dye (DiI)-stained hippocampal slices of CAP2- and control GFP-injected APP/PS1 mice. No changes in spine density or the length and width of the spines were detected (Figure 3A; Table 1). The evaluation of spine morphology revealed that different spine categories (mushroom, stubby, thin, and filopodia) were associated with CAP2 overexpression in preliminary analysis (Figure 3A, chi-square test, $p < 0.0001$); this result was confirmed when we separately treated (1) stubby spines (reference category) and mushroom spines (Figure 3A, chi-square test on the restricted table, $p < 0.0001$); (2) thin spines (reference category) and mushroom spines (Figure 3A, chi-square test on the restricted table, $p < 0.001$); (3) non-mushroom spines (reference category including filopodia, thin, and stubby spines) and mushroom spines (Figure 3A, chi-square test on the restricted table, $p < 0.0001$). However, when the hierarchical structure was modeled within each of the three generalized linear mixed-effects models (logit link function and binomial family), the treatment effect was no longer significant (Figure 3A, odds ratio and corresponding confidence intervals).

Even though the results of spine morphology analysis did not show any significant differences, analysis of the cAMP-responsive element-binding protein (CREB) signaling pathway, essential for synaptic plasticity,[26] revealed an increase in the phosphorylation of CREB at Ser^{133} in hippocampal homogenates of CAP2-injected mice compared with the control group (Figure 3B). These data indicate that increasing CAP2 levels in the hippocampus of AD mice significantly induced CREB activation signaling, promoting synaptic plasticity.

In addition, we assessed the effect of CAP2 overexpression on cytoskeleton abnormalities related to AD synaptic degeneration, such as tau phosphorylation at Thr^{181} (pTau-181),[27] which has been reported to be increased in 6-month-old APP/PS1 mice,[28] and cofilin-actin rod deposition in the hippocampus of AD mice.

CAP2-injected APP/PS1 mice or the control group. The statistical analysis shows that the ratio between pCREB and CREB total levels is increased in CAP2 mice (AAV-GFP = 100 ± 2.761, AAV-mycCAP2 = 185.2 ± 39.57; two-tailed unpaired t test: $^*p = 0.02$, $n = 9$–10 mice). (C) Representative immunoblotting experiment of homogenates derived from hippocampal tissue of APP/PS1 mice receiving AAV-mycCAP2 vector or the control. Quantitative analysis of pTau181 OD and normalization to Tau OD suggests that pTau181 levels are significantly reduced in the hippocampus of CAP2-injected mice (AAV-GFP = 100 ± 3.932, AAV-mycCAP2 = 86.8 ± 6.406; two-tailed unpaired t test: $^*p = 0.0496$, $n = 8$–10 mice). (D) Confocal representative images of 6-month-old AAV-mycCAP2 (or AAV-GFP) APP/PS1 brains subjected to immunohistochemistry for cofilin (violet) and DAPI (cyan); right panels, inverted images of cofilin-actin rods (white) detected in coronal section of CAP2 (or GFP)-injected APP/PS1 mice hippocampus. Scale bar, 50 μm. The graphs show decreased cofilin-actin rod formation (expressed as number and total area of actin rods) in CAP2-injected APP/PS1 mice compared with the control animals (number of actin rods, AAV-GFP = 100 ± 4.108, AAV-mycCAP2 = 69.49 ± 4.233; two-tailed nested t test for number of actin rods AAV-GFP vs. AAV-mycCAP2 $^{**}p = 0.0037$, $n = 5$ mice; total area of actin rods, AAV-GFP = 100 ± 4.498, AAV-mycCAP2 = 71.59 ± 4.948; two-tailed nested t test for total area of actin rods AAV-GFP vs. AAV-mycCAP2 $^*p = 0.0372$, $n = 5$ mice). (E) Immunohistochemical labeling of Aβ plaques (magenta) using the 6E10 antibody in representative confocal images of hippocampal coronal sections from APP/PS1 mice injected with AAV-mycCAP2 or control AAV-GFP. Scale bar, 200 μm. Quantification shows that both the number and area of plaques (normalized to hippocampal area) are unchanged between the two groups (number of plaques/area hippocampus, AAV-GFP = 100 ± 11.68, AAV-mycCAP2 = 70.49 ± 13.78; two-tailed nested t test for number of plaques n.s. (non-significant), $p = 0.2703$, $n = 7$–8 mice; area of plaques/area hippocampus, AAV-GFP = 100 ± 14.79, AAV-mycCAP2 = 78.89 ± 17.02; two-tailed nested t test for area of plaques n.s. (non-significant), $p = 0.4316$, $n = 7$–8 mice). All data are presented as the percentage of control AAV-GFP-injected mice and expressed as mean ± SE.

Table 1. Beta coefficient estimates, and corresponding standard errors and *p* values from fixed-effects and robust or mixed-effects models with reference to the corresponding figures

Figure	Dependent variable	Random effects at different hierarchical levels: Neuron	Independent variable[a,b]	Estimate	Standard error	Wald *p* value[g]	ANOVA *p* value[g]
3A	Spine density	N_Animals = 10, STD Animal = 1.623 N_Images = 2–3 per Animal, STD Image = 2.215	Treatment (AAV-mycCAP2 vs. AAV-GFP)	0.688	1.234	0.593	0.593
	Spine length	N_Animals = 10, STD Animal = 0.029 N_Images = 4–9 per Animal, STD Image = 0.082 N_Dendrites = 1–5 per Animal and Image, STD Dendrite = 0.071	Treatment (AAV-mycCAP2 vs. AAV-GFP)	0.011	0.031	0.734	0.734
	Spine width	N_Animals = 10, STD Animal = 0.023 N_Images = 4–9 per Animal, STD Image = 0.042 N_Dendrites = 1–5 per Animal and Image, STD Dendrite = 0.059	Treatment (AAV-mycCAP2 vs. AAV-GFP)	−0.005	0.021	0.798	0.798
S4A	Number of rods/neuron area	–	Treatment (oA$\beta_{1\text{-}42}$ vs. A$\beta_{42\text{-}1}$)	0.0026	0.0008	**0.001****	**0.005****
			Culture	–	–	–	0.070
			2 vs. 1	−0.0017	0.0010	0.079	–
			3 vs. 1	−0.0026	0.0010	**0.0095*****	–
	Area of rods/neuron area	–	Treatment (oA$\beta_{1\text{-}42}$ vs. A$\beta_{42\text{-}1}$)	0.0064	0.0014	**<0.0001*****	**<0.0001*****
			Culture	–	–	–	**0.086**
			2 vs. 1	−0.0035	0.0017	**0.044***	–
			3 vs. 1	−0.0038	0.0017	**0.031***	–
S5B	IntDen Cofilin/IntDen GFP	*N* = 5 or 12[c] STD = 0.096	Treatment (oA$\beta_{1\text{-}42}$ vs. A$\beta_{42\text{-}1}$)	−0.191	0.049	**0.0009*****	**0.0009*****
			Culture (2 vs. 1)	0.011	0.049	0.829	0.829
4D	Actin rods volume	*N* = 4 or 5[d] STD = 0.339	CAP2 status (positive vs. negative)	1.253	0.219	**<0.0001*****	**<0.0001*****
			Culture (2 vs. 1)	0.502	0.332	0.174	0.174
	Actin rods sphericity	*N* = 4 or 5[d,e]	CAP2 status (positive vs. negative)	−0.049	0.011	**<0.0001*****	**<0.0001*****
			Culture (2 vs. 1)	0.016	0.013	0.193	0.193
			Neuron	–	–	–	0.071
			2 vs. 1	0.027	0.018	0.140	–
			3 vs. 1	−0.000	0.014	0.988	–
			4 vs. 1	−0.002	0.018	0.894	–
			5 vs. 1	0.031	0.018	0.084	–
5D	PLA cluster density (30 min)	–	Treatment (oA$\beta_{1\text{-}42}$ vs. A$\beta_{42\text{-}1}$)	−0.032	0.008	<0.0001***	0.025**
			Culture	–	–	–	**0.085**

(*Continued on next page*)

Table 1. *Continued*

Figure	Dependent variable	Random effects at different hierarchical levels: Neuron	Independent variable[a,b]	Estimate	Standard error	Wald *p* value[g]	ANOVA *p* value[g]
			2 vs. 1	0.0191	0.0103	0.083	–
			3 vs. 1	0.0186	0.0130	0.176	–
			4 vs. 1	0.0205	0.0095	0.026*	–
							–
5E	PLA cluster density (24 h)	–	Treatment ($oA\beta_{1\text{-}42}$ vs. $A\beta_{42\text{-}1}$)	−0.0439	0.0077	**<0.0001*****	**<0.0001*****
			Culture	–	–	–	**0.0008*****
			2 vs. 1	−0.0002	0.0094	0.980	–
			3 vs. 1	0.0326	0.0093	**0.0008*****	–
6B	PLA cluster density	–	Treatment ($oA\beta_{1\text{-}42}$ vs. $A\beta_{42\text{-}1}$)	−0.0170	0.0912	0.853	0.802
			Culture	–	–	–	0.641
			2 vs. 1	−0.0181	0.1111	0.871	–
			3 vs. 1	0.0363	0.1083	0.739	–
6C	Number of rods/neuron area	–	Genetic treatment	–	–	–	**0.002****
			mycCAP2 C32G + $oA\beta_{1\text{-}42}$ vs. $A\beta_{42\text{-}1}$	0.0010	0.0014	0.511	–
			mycCAP2 FL + $oA\beta_{1\text{-}42}$ vs. $A\beta_{42\text{-}1}$	0.0007	0.0012	0.583	–
			$oA\beta_{1\text{-}42}$ vs. $A\beta_{42\text{-}1}$	0.0046	0.0012	**0.0003*****	–
			Culture	–	–	–	**0.007****
			2 vs. 1	0.0052	0.0014	**0.0002*****	–
			3 vs. 1	0.0020	0.0013	0.137	–
			4 vs. 1	0.0015	0.0013	0.265	–
	Area of rods/neuron area	–	Genetic treatment	–	–	–	**0.012***
			mycCAP2 C32G + $oA\beta_{1\text{-}42}$ vs. $A\beta_{42\text{-}1}$	0.0028	0.0024	0.239	–
			mycCAP2 FL + $oA\beta_{1\text{-}42}$ vs. $A\beta_{42\text{-}1}$	0.0009	0.0020	0.655	–
			$oA\beta_{1\text{-}42}$ vs. $A\beta_{42\text{-}1}$	0.0058	0.0021	**0.006****	–
			Culture	–	–	–	**0.009****
			2 vs. 1	0.0067	0.0022	**0.004****	–
			3 vs. 1	0.0013	0.0022	0.540	–
			4 vs. 1	0.0023	0.0021	0.276	–
6D	Spine density[f]	–	Genetic treatment	–	–	–	**<0.0001*****
			mycCAP2 C32G + $oA\beta_{1\text{-}42}$ vs. $A\beta_{42\text{-}1}$	−0.1136	0.0409	**0.007****	–
			mycCAP2 FL + $oA\beta_{1\text{-}42}$ vs. $A\beta_{42\text{-}1}$	−0.0460	0.0406	0.260	–

(*Continued on next page*)

Please cite this article in press as: Stringhi et al., Cyclase-associated protein 2 gene delivery: A potential multi-target approach for preventing synaptic failure in Alzheimer's disease, Molecular Therapy (2025), https://doi.org/10.1016/j.ymthe.2025.12.023

Table 1. *Continued*

Figure	Dependent variable	Random effects at different hierarchical levels: Neuron	Independent variable[a,b]	Estimate	Standard error	Wald *p* value[g]	ANOVA *p* value[g]
			oA$\beta_{1\text{-}42}$ vs. A$\beta_{42\text{-}1}$	−0.1925	0.0390	**<0.0001*****	–
			Culture	–	–	–	**0.0001*****
			2 vs. 1	0.1433	0.0346	**<0.0001*****	–
			3 vs. 1	0.0946	0.0335	**0.006****	–

Estimates, standard errors, and Wald *p* values were obtained with rlm and f.robftest functions; ANOVA *p* value for robust regression was obtained with lmRob and its robust ANOVA estimator.
ANOVA, analysis of variance; *N*, number of neurons; STD, standard deviation.
[a]For practical purposes there must be a reasonable number of random-effects levels (i.e., at least five) to provide the readers with valid effect estimates from mixed-effect models. For this reason, we decided to treat *culture* (at most four levels) as a fixed effect in any model fitted in the current paper; as it mostly reached five levels, *neuron* was treated as a random effect, except when convergence issues arose.
[b]For each figure and dependent variable, specified independent variables were simultaneously included in the model and were thus mutually adjusted the one for the other(s).
[c]Number of neurons was 5 for culture number 1 and 12 for culture number 2.
[d]Number of neurons was 4 for culture number 1 and 5 for culture number 2.
[e]Due to convergence issues, fixed-effects terms were introduced instead of the corresponding mixed-effects ones for neurons.
[f]Number of observations was 88 (33 NA for spine density analyses).
[g]Statistically significant *p*-values are shown in bold.

We found a significant reduction of tau phosphorylation at Thr^{181}, without changes in the total levels of tau, in the hippocampus of CAP2-injected mice compared with GFP-injected controls (Figure 3C). This suggests that CAP2 overexpression ameliorates a tau-related pathological trait in AD mice. Concerning cofilin-actin rod deposition, several studies have previously provided evidence that Aβ induces rod aggregation, primarily in the dentate gyrus (DG) of hippocampal region.[4,6,29] We stained hippocampal coronal sections with an antibody for cofilin to detect cofilin-actin rods and performed quantitative analysis in the DG. We observed a significant reduction of both the number and total area of actin rods in the DG of CAP2-injected mice compared with GFP-injected controls, confirming that CAP2 overexpression prevented cofilin-actin rod formation in APP/PS1 mice (Figure 3D). To determine whether CAP2 overexpression prevents the deposition of amyloid plaques, we quantified both the number and total area of hippocampal plaques in APP/PS1 mice following injection with either CAP2 or control GFP vectors. Analysis revealed no significant differences in plaque burden between CAP2-injected and control groups, suggesting that CAP2 overexpression does not influence amyloid accumulation in this model (Figure 3E).

CAP2 is specifically sequestered within Aβ-induced mature cofilin-actin rods

Given the strict cooperation between CAP2 and cofilin[20] and the data indicating that CAP2 overexpression protects neuronal cells from actin rod formation (Figure 3D), we further investigated the role of CAP2 in cofilin-actin rod assembly. Although cofilin-actin rods are described as aggregates composed of cofilin and actin, mass spectrometric proteomic analysis of these structures has suggested contamination with other actin-related proteins.[30] For this reason, we investigated whether CAP2 could be sequestered within these cytoplasmic aggregates.

To address this issue, we set up and validated an *in vitro* experimental paradigm to study Aβ-dependent actin rod formation. We exposed primary hippocampal cultures to a well-characterized Aβ oligomer (oA$\beta_{1\text{-}42}$) preparation at a concentration of 500 nM for 24 h (Figure 4A); as a negative control, we used a peptide with the reverse sequence of Aβ (A$\beta_{42\text{-}1}$). It has been previously shown that a 24-h treatment leads to a loss of spines without affecting cell viability.[31] We observed a significant increase in actin rod deposition in neurons treated with oA$\beta_{1\text{-}42}$ for 24 h compared with the control (Figure S4A; Tables 1 and S2). Besides this, we also evaluated the effect of Aβ oligomer exposure on cofilin activation. The Lim kinase phosphorylates cofilin on Ser^{3}, inactivating it; consistent with several publications,[32,33] we found an aberrant increase in cofilin phosphorylation upon oA$\beta_{1\text{-}42}$ treatment, corresponding to an inactivation of the protein (Figure S4B). Overall, these data support the feasibility of our *in vitro* model to investigate the effects of oA$\beta_{1\text{-}42}$ on the CAP2/cofilin pathway.

To evaluate whether CAP2 is localized within cofilin-actin rods, we stained hippocampal neurons for CAP2 and for cofilin to detect the

Please cite this article in press as: Stringhi et al., Cyclase-associated protein 2 gene delivery: A potential multi-target approach for preventing synaptic failure in Alzheimer's disease, Molecular Therapy (2025), https://doi.org/10.1016/j.ymthe.2025.12.023

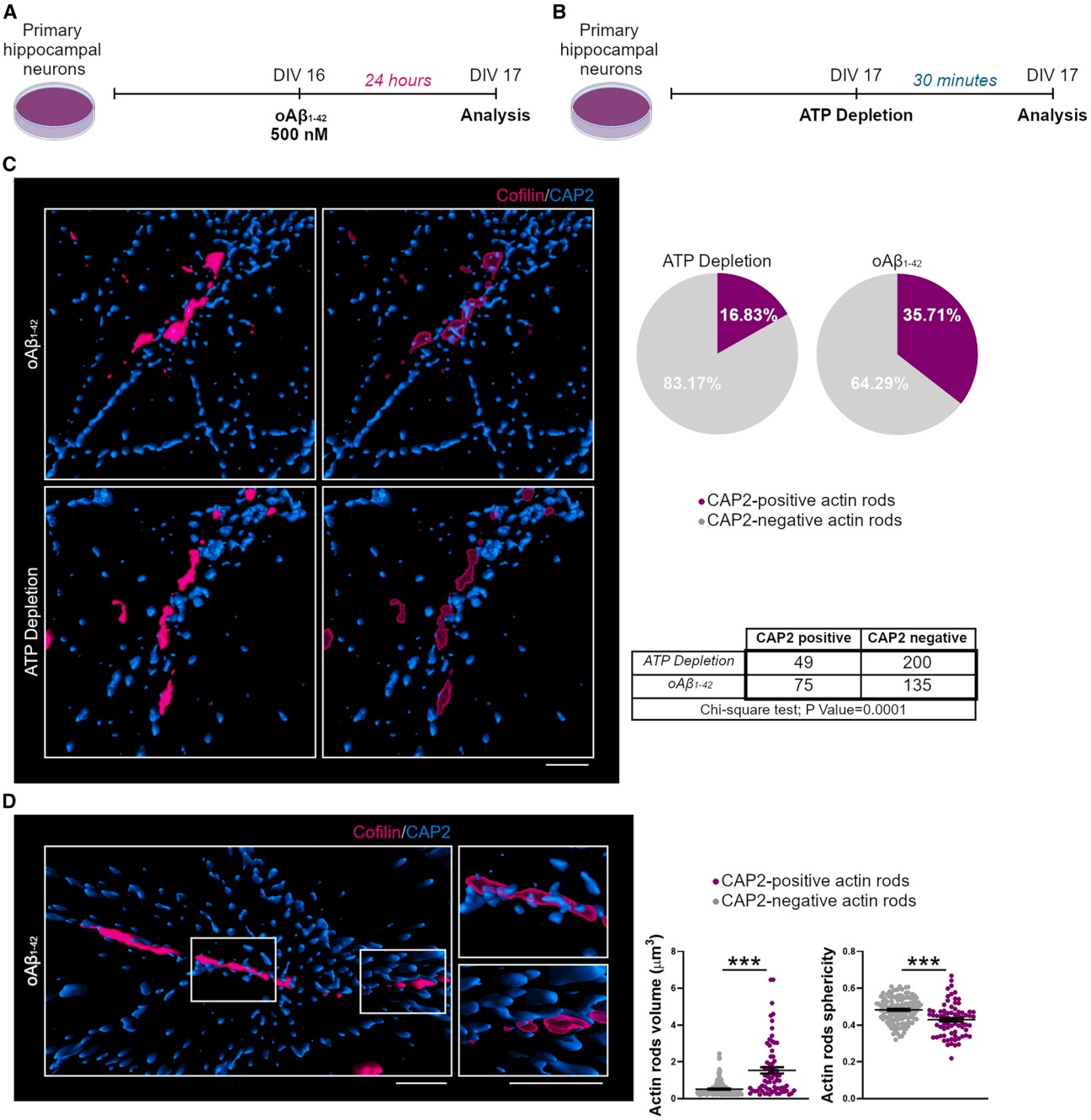

Figure 4. Amyloid-β oligomer exposure induces CAP2 recruitment within cofilin-actin rods and its accumulation in bigger and elongated aggregates

(A) Graphical representation of the experimental treatment scheme: rat primary hippocampal neurons at 16 days *in vitro* (DIV 16) were exposed to 500 nM of Aβ oligomers ($oA\beta_{1-42}$) for 24 h. (B) Schematic representation of ATP depletion treatment: hippocampal neurons were subjected to ATP depletion medium (10 mM sodium azide, 6 mM 2-deoxyglucose) for 30 min. (C) Representative images of 3D projection of cofilin-actin rods (magenta) and the endogenous levels of CAP2 (cyan). Scale bar, 2 μm. The graphs show a significant increase in the percentage of CAP2-positive actin rods after $oA\beta_{1-42}$ treatment compared with ATP depletion. The joint distribution of actin rod population and treatment is represented in the table together with the *p* value of the chi-square test ($p = 0.0001$). (D) Representative 3D reconstruction of actin rods (magenta) induced by $oA\beta_{1-42}$ treatment and the endogenous levels of CAP2 (cyan). Scale bar: overview, 2 μm; zoom, 500 nm. The quantitative analysis of the cofilin-actin rod population highlights a higher volume and lower sphericity of CAP2-positive actin rods (data in the graph are presented as percentage of CAP2-negative actin rods, *p* value provided in Table 1 and adjusted means and SE provided in Table S2).

Please cite this article in press as: Stringhi et al., Cyclase-associated protein 2 gene delivery: A potential multi-target approach for preventing synaptic failure in Alzheimer's disease, Molecular Therapy (2025), https://doi.org/10.1016/j.ymthe.2025.12.023

actin rods after 24 h of treatment with oAβ_{1-42}. We performed a three-dimensional colocalization analysis to measure the amount of CAP2 contained within these aggregates. As shown in the representative images (Figure 4C), incubation with oligomers induced the formation of 35.71% CAP2-positive actin rods, defined as rods with CAP2 signal overlapping 100% with cofilin rods signal. To assess the specificity of our results, we took advantage of a validated small hairpin RNA (shRNA) to down-regulate CAP2 expression (Figure S4C).[20] The three-dimensional colocalization analysis revealed a significant reduction in the number of CAP2-positive cofilin-actin rods in neuronal cells transfected with CAP2-shRNA compared with control cells (16.11%, Figure S4C). To test whether another stressor can induce the formation of CAP2-positive actin rods, we compared the effect of oAβ_{1-42} treatment with a well-characterized ATP depletion protocol able to generate actin rods (Figure 4B).[5] Interestingly, the analysis revealed that the percentage of CAP2-positive actin rods formed upon application of the ATP depletion protocol (16.83%, Figure 4C) was similar to those detected in CAP2 shRNA-transfected cells (16.11%, Figure S4C), but lower than the percentage observed following the oAβ_{1-42} treatment (35.71%, Figure 4C). We then analyzed the structure of CAP2-containing actin rods. The results show that CAP2-positive actin rods have a higher volume and lower sphericity compared with CAP2-negative actin rods (Figure 4D; Tables 1 and S2). These results suggest that CAP2 preferentially accumulates within bigger and more elongated structures, indicative of processes occurring during the late stages of actin rod maturation.

Taken together, these results suggest that CAP2 accumulation within actin rods is more prominent under Aβ-induced stress and that CAP2 preferentially localizes to rods with specific morphological features.

The CAP2-cofilin pathway is a target of the initial events induced by exposure to Aβ oligomers

We next set out to assess the effect of oAβ_{1-42} treatment on CAP2/cofilin synaptic mechanisms using our *in vitro* model. We treated primary hippocampal neurons with oAβ_{1-42} and performed analysis of CAP2 and cofilin levels in the postsynaptic compartment after either 30 min or 24 h of exposure (Figure 5A). We focused on these time points to examine both the initial synaptic events triggered by oAβ_{1-42} and to provide a snapshot of the CAP2/cofilin synaptic pathway at the point when spine loss and actin rod formation occur (i.e., at 24 h).

As shown in Figure 5B, the short-term exposure to oAβ_{1-42} significantly decreased both CAP2 and cofilin levels in the postsynaptic TIF, without affecting levels of the two proteins in the total homogenate (Figure S5A). To further confirm the effect of oAβ_{1-42} on cofilin localization, we employed an imaging approach. GFP-transfected hippocampal neurons were incubated with oAβ_{1-42} and were then stained for cofilin. We took advantage of structured illumination microscopy (SIM) to measure the relative concentration of cofilin in the spine by dividing cofilin intensity by GFP signal.[11] As shown in Figure S5B (Tables 1 and S2), fluorescence analysis confirmed that a short-term oAβ_{1-42} treatment decreases cofilin synaptic availability. The 24-h oAβ_{1-42} treatment revealed a significant decrease in cofilin synaptic localization, while no alterations in CAP2 synaptic levels were detected (Figure 5C). As reported in Figure S5C, even a 24-h oAβ_{1-42} incubation did not affect the total expression of CAP2 and cofilin.

Then, we tested the effect of oAβ_{1-42} on CAP2/cofilin association and CAP2 homodimer formation. To detect CAP2/cofilin complexes, we performed a proximity ligation assay (PLA) in hippocampal neurons. When cofilin and CAP2 are in close proximity (<40 nm), a PLA signal can be detected. In neurons treated with oAβ_{1-42} (500 nM) for both 30 min and 24 h, the density of PLA signals was significantly reduced when compared with Aβ_{42-1}-treated cells (Figures 5D and 5E; Tables 1 and S2). Concerning CAP2 homodimer formation, quantitative analysis of the CAP2 dimer levels showed no significant impairment of CAP2 dimerization in the total homogenate or the postsynaptic compartment upon 30-min exposure to oAβ_{1-42} compared with the control condition (Figures S5D and 5F). On the other hand, 24 h of oAβ_{1-42} treatment significantly impaired the capability of CAP2 to dimerize in the postsynaptic compartment of hippocampal neurons (Figure 5G). Interestingly, the levels of CAP2 dimer in the total homogenate remained unchanged (Figure S5E), as observed in AD patients and APP/PS1 mice,[20] suggesting that only CAP2 dimerization in the synapse is affected by oAβ_{1-42}. These data suggest that CAP2/cofilin association is already impaired after a short exposure to oAβ_{1-42}, even before the dimer levels are affected, while upon 24 h of oAβ_{1-42} treatment, CAP2 dimerization is completely disrupted in the synapse. Overall, these data show that synaptic CAP2, cofilin, and their association are early targets of oAβ_{1-42}; CAP2 synaptic homodimerization, required for the plasticity-induced remodeling of spines,[20] is profoundly affected after longer oAβ_{1-42} treatment.

CAP2 dimerization is essential for preventing Aβ-induced dendritic spine loss but is not necessary for protection against cofilin-actin rod formation

Considering that long-term exposure to oAβ_{1-42} affects synaptic levels of the CAP2 dimer, we examined the role of CAP2 overexpression and dimerization in an *in vitro* model.

To do this, at day *in vitro* 10 (DIV10) we transfected primary hippocampal neurons with a plasmid expressing mCherry, used as a filler, and either full-length mycCAP2 (mycCAP2 FL) or a mutant carrying Cys^{32} mutated to Glycine, that is not able to dimerize (mycCAP2-C32G).[20] At DIV16 transfected neurons were exposed to oAβ_{1-42} for 24 h (Figure 6A). First, we performed a PLA assay in neurons overexpressing mycCAP2 and treated with either oAβ_{1-42} or the control oAβ_{42-1} for 24 h. The analysis of the number of PLA clusters revealed no significant difference between the two experimental groups (Figure 6B; Tables 1 and S2), confirming the efficacy of CAP2 overexpression in preventing the oAβ_{1-42}-induced decrease in CAP2-cofilin association (Figure 5E).

Please cite this article in press as: Stringhi et al., Cyclase-associated protein 2 gene delivery: A potential multi-target approach for preventing synaptic failure in Alzheimer's disease, Molecular Therapy (2025), https://doi.org/10.1016/j.ymthe.2025.12.023

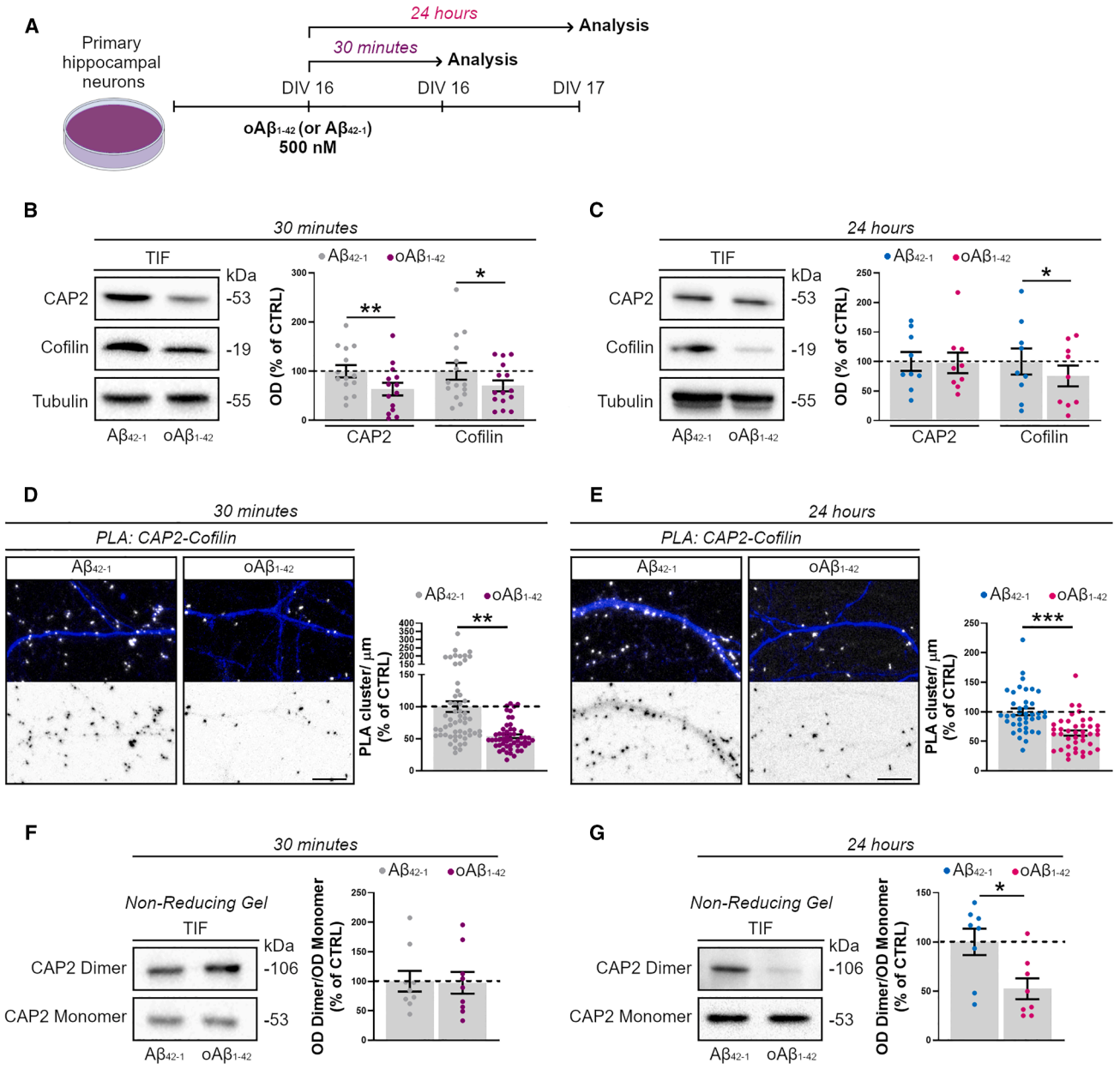

Figure 5. Amyloid-β oligomer treatment affects the CAP2-cofilin pathway after both short and chronic exposures

(A) Experimental design: rat hippocampal neurons (DIV 16) were treated with 500 nM Aβ oligomers ($oAβ_{1-42}$) or control peptide ($Aβ_{42-1}$) for 30 min or 24 h before analysis. (B) WB of postsynaptic TIF from hippocampal cultures exposed to $oAβ_{1-42}$ or $Aβ_{42-1}$ for 30 min. CAP2 and cofilin synaptic localization was decreased after $oAβ_{1-42}$ treatment (CAP2, $Aβ_{42-1}$ = 100 ± 12.61, $oAβ_{1-42}$ = 63.60 ± 12.84, cofilin, $Aβ_{42-1}$ = 100 ± 17.17, $oAβ_{1-42}$ = 70.37 ± 11.06; two-tailed paired *t* test: CAP2, $oAβ_{1-42}$ vs. $Aβ_{42-1}$ $^{**}p = 0.0075$; cofilin, $oAβ_{1-42}$ vs. $Aβ_{42-1}$ $^{*}p = 0.0307$, n = 14–15). (C) Immunoblot analysis of TIF samples after 24-h exposure to $oAβ_{1-42}$. Cofilin synaptic localization was reduced, while CAP2 levels remained unchanged (CAP2, $Aβ_{42-1}$ = 100 ± 15.98, $oAβ_{1-42}$ = 97.71 ± 17.42, cofilin, $Aβ_{42-1}$ = 100 ± 22.12, $oAβ_{1-42}$ = 75.49 ± 17.67; two-tailed paired *t* test: CAP2, $oAβ_{1-42}$ vs. $Aβ_{42-1}$ n.s. (non-significant), $p = 0.8382$; cofilin, $oAβ_{1-42}$ vs. $Aβ_{42-1}$ $^{*}p = 0.0218$, n = 9). (D) Confocal images of PLA revealed decreased CAP2–cofilin interaction (white) in MAP2-positive dendrites (blue) of neurons treated with $oAβ_{1-42}$ for 30 min ($Aβ_{42-1}$ = 100 ± 8.422, $oAβ_{1-42}$ = 53.83 ± 2.953; *p* values are reported in Table 1 and adjusted means and SE provided in Table S2). Scale bar, 5 µm. (E) PLA analysis revealed that CAP2-cofilin binding is affected after 24-h $oAβ_{1-42}$ treatment ($Aβ_{42-1}$ = 100 ± 5.609, $oAβ_{1-42}$ = 63.86 ± 4.410; *p* values are reported in Table 1 and adjusted means and SE provided in Table S2). Scale bar, 5 µm. (F) Non-reducing gels of the postsynaptic fraction revealed unchanged CAP2 dimer/monomer ratios after 30-min $oAβ_{1-42}$ exposure (CAP2, $Aβ_{42-1}$ = 100 ± 17.47, $oAβ_{1-42}$ = 97.40 ± 18.44; two-tailed paired *t* test: CAP2, $oAβ_{1-42}$ vs. $Aβ_{42-1}$ n.s. (non-significant), $p = 0.7716$, n = 9). (G) After 24 h of $oAβ_{1-42}$ exposure, CAP2 dimerization was significantly reduced (CAP2, $Aβ_{42-1}$ = 100 ± 13.50, $oAβ_{1-42}$ = 52.39 ± 10.64; two-tailed paired *t* test: CAP2, $oAβ_{1-42}$ vs. $Aβ_{42-1}$ $^{*}p = 0.0112$, n = 8). All data are presented as percentages of control peptide $Aβ_{42-1}$ treated cells and expressed as mean ± SE.

Please cite this article in press as: Stringhi et al., Cyclase-associated protein 2 gene delivery: A potential multi-target approach for preventing synaptic failure in Alzheimer's disease, Molecular Therapy (2025), https://doi.org/10.1016/j.ymthe.2025.12.023

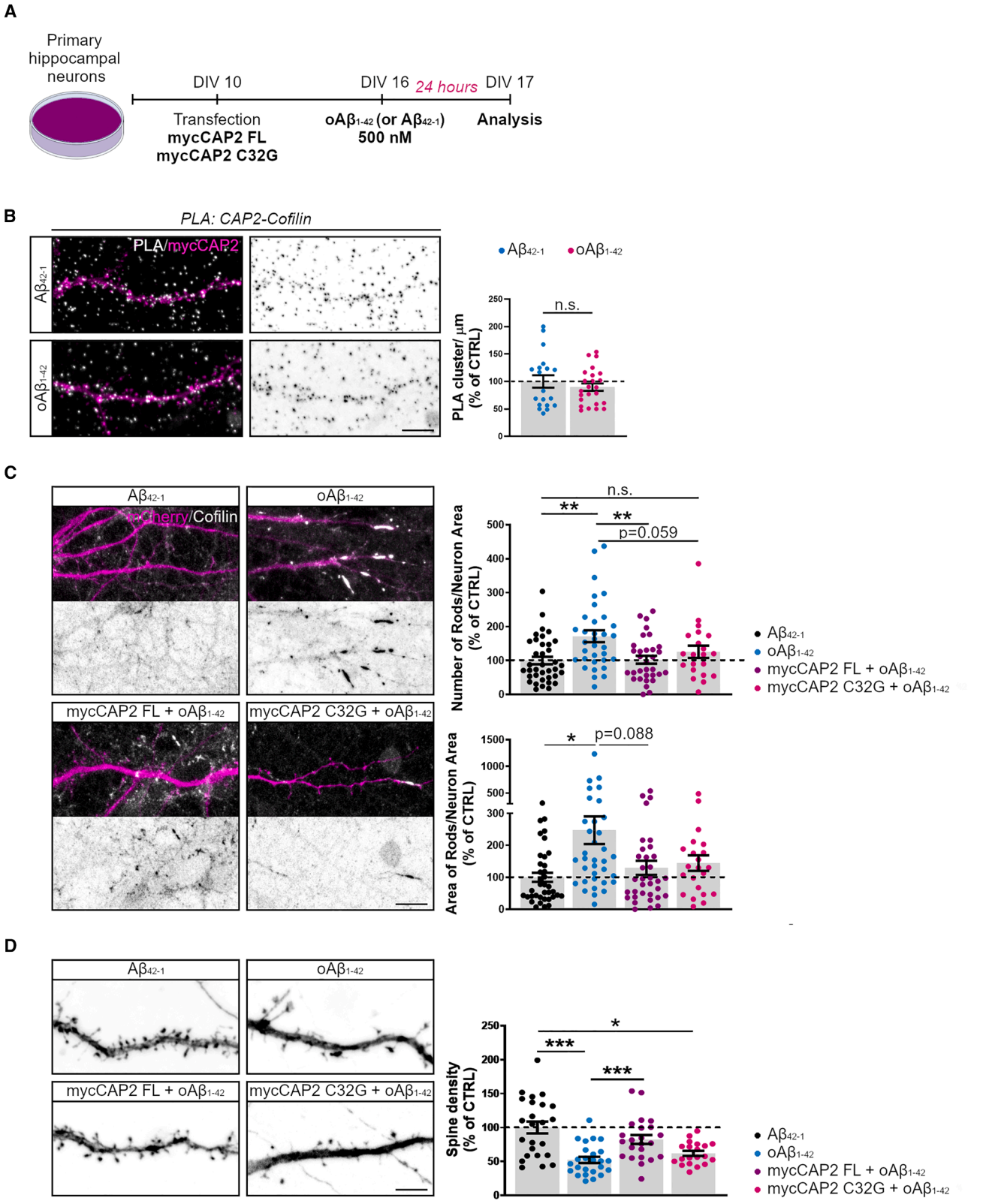

(legend on next page)

Please cite this article in press as: Stringhi et al., Cyclase-associated protein 2 gene delivery: A potential multi-target approach for preventing synaptic failure in Alzheimer's disease, Molecular Therapy (2025), https://doi.org/10.1016/j.ymthe.2025.12.023

Then, we tested the effect of mycCAP2 overexpression on actin rod generation and spine loss. We observed a significant decrease in the number of actin rods generated in oAβ_{1-42}-exposed neurons when CAP2 was overexpressed (Figure 6C; Tables 1, S2, and S3). The analysis of actin rod area revealed a trend for reduction, although not significant, in mycCAP2-overexpressing neurons exposed to oAβ_{1-42} compared with control cells treated with oAβ_{1-42} (mycCAP2 FL + oAβ_{1-42} vs. oAβ_{1-42}, p = 0.088; Figure 6C; Table S3). Furthermore, the analysis of spine density revealed that in CAP2-overexpressing hippocampal neurons, oAβ_{1-42} treatment did not trigger spine loss (Figure 6D; Tables 1, S2, and S3).

Interestingly, overexpression of the mutant lacking the capability to dimerize showed different results concerning actin rod formation and spine degeneration. We measured a trend toward reduction in the number of actin rods in neurons expressing mycCAP2 C32G mutant and exposed to oAβ_{1-42} when compared with control cells oAβ_{1-42}-treated (mycCAP2 C32G + oAβ_{1-42} vs. oAβ_{1-42}, p = 0.059; Figure 6C; Table S3). No differences were detected when compared with control-treated cells exposed to the peptide with the reverse Aβ sequence (mycCAP2 C32G + oAβ_{1-42} vs. Aβ_{42-1}, p = 0.914; Figure 6C; Table S3). These data suggest that the capability of CAP2 to form Cys^{32}-dependent dimers is not essential to protect the neurons from actin rod generation. However, the transfection of the C32G mutant did not prevent spine loss, since we observed a significant reduction in dendritic spine density in mycCAP2-C32G expressing neurons (mycCAP2 C32G + oAβ_{1-42} vs. Aβ_{42-1}, p = 0.022; Figure 6D; Table S3). Our results demonstrate that CAP2 Cys^{32}-dependent homodimerization is an essential mechanism that is required to protect dendritic spines from Aβ-induced synaptotoxicity but is not crucial for preventing cofilin-actin rod generation.

DISCUSSION

In this study, our findings highlight CAP2 as a player in the formation of cofilin-actin rods, which have been mainly implicated in cognitive impairments in AD.[5,34] The formation of cofilin-actin rods is central to cytoskeleton dysregulation in neurodegenerative disorders,[35–37] and a growing body of evidence points to their potential as a therapeutic target.[38,39] Here, combining *in vitro* and *in vivo* approaches, we demonstrate the following: (1) CAP2 is an early synaptic target of oAβ_{1-42} and a component of oAβ_{1-42}-induced cofilin-actin rod formation; (2) CAP2 overexpression in a mouse model of amyloid pathology counteracts the formation of cofilin-actin rods and tau abnormalities without affecting plaque deposition, preserves the CAP2/cofilin synaptic complex and plasticity-related pathways, and, thereby, prevents the onset of cognitive defects; and (3) Cys^{32}-dependent CAP2 dimerization is required to ameliorate spine deficits but not for preventing cofilin pathology.

Cofilin dysregulation has previously been associated with several pathological AD traits. Cofilin-actin rods were shown to interfere with intracellular trafficking, induce synaptic loss,[40] disrupt synaptic structure,[41] and promote the reorganization and sequestering of phospho-tau.[42] Cofilin activities are spatiotemporally orchestrated by numerous extra- and intracellular factors. Among them, we focused our attention on CAP2 as a binding partner that controls cofilin synaptic abundance through the formation of Cys^{32} CAP2 homodimers and is required for spine structural changes triggered by LTP.[20] Furthermore, CAP2 levels are reduced in the hippocampus of AD patients and APP/PS1 mice at the early stages of the disease.[20] In line with these results, CAP2 downregulation has been validated in the NeuroPro database. Given these findings, we explored whether increasing CAP2 expression in APP/PS1 mice could serve as a potential strategy to prevent amyloid-triggered synaptic failure and cognitive decline.

Current therapeutic options for AD are mainly symptomatic. Only recently the Food and Drug Administration has approved the disease-modifying passive immunization therapies lecanemab and donanemab, monoclonal antibodies that reduce the amyloid plaque burden and slow cognitive decline. However, questions have been raised about both the clinical efficacy and safety of these therapies.[43] Thus, a lot of effort is being made to develop different approaches to combine with anti-amyloid immunotherapies.

Here, we show that specific AAV-mediated gene delivery of CAP2 in the neurons of the hippocampus of APP/PS1 mice in the early asymptomatic stages of the disease prevents the onset of cognitive deficits. CAP2-overexpressing APP/PS1 mice maintain intact spatial and recognition memory compared with control APP/PS1 mice, as

Figure 6. CAP2 overexpression in primary hippocampal neurons prevents the Aβ-triggered disruption of CAP2-cofilin association, actin rod generation, and dendritic spine failure

(A) Experimental procedures: hippocampal neurons were transfected with vectors expressing mCherry, and either full-length mycCAP2 (mycCAP2 FL) or mycCAP2 C32G vectors, then exposed to oAβ_{1-42} (or Aβ_{42-1}) for 24 h. (B) Confocal images of PLA signal deriving from CAP2-cofilin association (white), performed on neurons transfected with mCherry and overexpressing mycCAP2 FL (magenta) and exposed to oAβ_{1-42} (or Aβ_{42-1}) for 24 h. Scale bar, 10 μm. Quantitative analysis shows that CAP2 overexpression prevents oAβ_{1-42}-induced alteration on CAP2-cofilin interaction (Aβ_{42-1} = 100 ± 11.34, oAβ_{1-42} = 89.62 ± 6.698; p values are reported in Table 1 and adjusted means and SE provided in Table S2). (C) Confocal images of actin rod staining (white) in primary hippocampal neurons. Scale bar, 20 μm. The analysis (number of rods/area of the neuron and area of rods/area of the neuron) demonstrated that both mycCAP2 FL and mycCAP2 C32G overexpression reduced Aβ-induced actin rods formation (number of rods/area neuron; Aβ_{42-1} = 100 ± 10.94; oAβ_{1-42} 207.6 ± 30.60, mycCAP2 FL + oAβ_{1-42} = 122.4 ±18.01, mycCAP2 C32G + oAβ_{1-42} 141.7 ± 23.47; area of rods/area neuron; Aβ_{42-1} = 100 ± 14.16; oAβ_{1-42} 247.2 ± 43.37, mycCAP2 FL + oAβ_{1-42} = 129.5 ± 22.19, mycCAP2 C32G + oAβ_{1-42} 144.4 ± 24.14; adjusted means and SE provided in Table S2, p values and pairwise contrasts are reported in Tables 1 and S3). (D) Representative confocal images of dendrites and spines. Scale bar, 5 μm. Spine density analysis shows that oAβ_{1-42}-induced spine loss is prevented upon the overexpression of mycCAP2 FL (Aβ_{42-1} = 100 ± 8.790; oAβ_{1-42} 52.22 ± 4.495, mycCAP2 FL + oAβ_{1-42} = 90.31 ± 10.12, mycCAP2 C32G + oAβ_{1-42} 68.53 ± 5.699; adjusted means and SE provided in Table S2, p values and pairwise contrasts are reported in Tables 1 and S3). All data are presented as percentages of control peptide Aβ_{42-1} treated cells and expressed as mean ± SE.

Please cite this article in press as: Stringhi et al., Cyclase-associated protein 2 gene delivery: A potential multi-target approach for preventing synaptic failure in Alzheimer's disease, Molecular Therapy (2025), https://doi.org/10.1016/j.ymthe.2025.12.023

shown by the spatial displacement task and NORT. Furthermore, restoring CAP2 levels improves cognitive flexibility. The Barnes maze reversal learning test revealed that CAP2-overexpressing APP/PS1 mice have a more flexible memory, effectively applying previously learned skills to new circumstances. Besides this, the analysis of the search strategies showed that CAP2-overexpressing APP/PS1 mice applied effective serial search strategies more frequently than control APP/PS1 animals at both 6 and 9 months of age.

At a molecular level, CAP2 neuronal overexpression mitigates different features of cofilin pathology in AD. Increasing CAP2 levels significantly reduces the number of cofilin-actin rods in the DG, the region of the hippocampus where they are predominantly induced by Aβ.[29] Considering that cofilin also plays an intermediary role in the neurotoxic signaling that promotes tauopathy,[42,44] we measured pTau-181, the most sensitive biomarker for predicting cognitive worsening at the prodromal AD stage.[45,46] Furthermore, our recent study revealed that CAP2 levels in the CSF undergo significant alterations starting in the AD prodromal phase and strongly correlate with tau-related pathological changes both in patients and in *in vitro* systems.[21] Notably, CAP2 downregulation in neuronal cultures significantly increases pTau-181 levels. Our results show that increasing CAP2 levels through overexpression reduces pTau-181 levels in the hippocampus of APP/PS1 mice, thus ameliorating cytoskeletal abnormalities found in AD, without affecting a key AD hallmark as plaques deposition.

The effect of CAP2 overexpression can also be detected at the synaptic level. Increasing CAP2 levels promotes CAP2 localization at the postsynaptic site and, more importantly, rises the synaptic abundance of Cys^{32}-dependent CAP2 homodimers and their association with cofilin. This represents a key mechanism that promotes cofilin synaptic availability and consequently restores the control of actin dynamics, which are both relevant for postsynaptic plasticity. In line with these results, we measured a significant increase in the phosphorylation of the transcription factor CREB at Ser^{133}, a key element coupling synaptic activation to the transcription of genes required for long-term synaptic plasticity events and memory formation.[26]

To further support the involvement of CAP2/cofilin association in AD synaptic failure, we found that this synaptic complex is a target of $oA\beta_{1\text{-}42}$. We used a preparation of $oA\beta_{1\text{-}42}$ able to induce synaptic depression in 30 min and spine loss in 24 h without causing cell death.[31] Although we have previously shown that long-term depression (LTD) does not affect CAP2 postsynaptic levels,[20] short-term $oA\beta_{1\text{-}42}$ treatment leads to a decrease in the postsynaptic availability of CAP2 and cofilin, without affecting postsynaptic Cys^{32}-dependent CAP2 homodimerization. These data suggest that short-term exposure to $oA\beta_{1\text{-}42}$ engages a maladaptive synaptic plasticity response that over 24 h of treatment leads to spine loss, cofilin-actin rod formation, and reduced synaptic availability of cofilin. The decreased synaptic levels of cofilin upon 24 h of exposure to $oA\beta_{1\text{-}42}$ may result in a decline in cofilin-mediated actin dynamics that negatively affects synaptic plasticity. The synaptic depletion of cofilin could be ascribed to a significant reduction of the CAP2 dimer in the synaptic compartment and cofilin sequestration by cofilin-actin rods, detectable along the dendrites. Indeed, when we overexpressed CAP2 in the hippocampus of APP/PS1 mice, we detected an increase in CAP2 dimer levels and synaptic cofilin availability along with a reduction in cofilin-actin rods.

In this context, we asked whether CAP2 contributes to the process of cofilin-actin rod formation since proteomic analysis has revealed the presence of many proteins in these intracellular inclusions.[30] To fully characterize cofilin-actin rods, we used three-dimensional imaging analysis and mixed-effects models; this approach enabled us to fully account for the complex design of multi-level, hierarchically structured imaging data[47] to control for variability at culture and neuron levels, providing us with more precise mean estimates.[48] This analysis revealed that CAP2 is a component of a subpopulation of cofilin-actin rods, specifically those that are bulkier and more elongated. Even though cofilin-actin rod formation can be triggered by different cellular stressors,[4] we detected a higher percentage of CAP2-positive actin rods forming in response to $oA\beta_{1\text{-}42}$ than to ATP depletion. These data support the hypothesis of a specific involvement of CAP2 in $oA\beta_{1\text{-}42}$-induced cofilin-actin rod formation.

Overall, our results point to CAP2 as a hub at the crossroads of pathogenic AD mechanisms related to synaptic loss and cofilin-actin rod formation. Interestingly, the results obtained in hippocampal cultures highlight the role of CAP2 in promoting cytoskeleton resilience to $oA\beta_{1\text{-}42}$ cellular stress via different mechanisms. Indeed, while CAP2 dimerization through Cys^{32} is required for protecting dendritic spines from $oA\beta_{1\text{-}42}$-induced synaptic loss, it is not necessary for preventing actin rod generation.

Our findings highlight CAP2 as a pivotal effector of synaptic resilience in AD, positioning the actin cytoskeleton as a promising therapeutic target for preventing synaptic dysfunction. Notably, sustained restoration of CAP2 expression in the hippocampus effectively blocks key molecular, structural, and cognitive manifestations of amyloid toxicity, without affecting Aβ plaque burden. Although the APP/PS1 mouse model does not fully capture the complexity of human AD, these results deepen our understanding of the molecular events leading to synaptic degeneration and chart a compelling path toward the development of next-generation synaptoprotective therapies.

MATERIALS AND METHODS

Human hippocampal postmortem specimens

The hippocampus of postmortem specimens obtained from AD patients and age-matched HCs were purchased from the Netherlands Brain Bank (NBB). AD tissues were categorized according to the established Braak and Braak criteria[49] and fulfilled stages 4 and 5; tangles and neuritic plaques were present in the hippocampi. HCs had no history of psychiatric or neurological disorders and no evidence of significant age-related neurodegeneration. Table S1 reports detailed information.

RNA extraction and RT-qPCR

RNA was extracted from hippocampal samples of AD patients and HCs using TRIZOL (Thermo Fisher Scientific), according to the supplier's specifications. RT-qPCR was performed with the iTaq Universal SYBR Green One-Step Kit (Bio-Rad, 1725151) using the CFX-384 well plate instrument (Bio-Rad). *CAP2* mRNA levels were normalized to the geometric mean of *H3-4* (encoding for Histone H3.4) and *ACTB* (encoding for β-Actin) levels.

The following oligos were used for qPCR analysis:

- *CAP2* FOR 5′-AAATGGTGCACAGTGCTTTCC -3′
- *CAP2* REV 5′-GGATGCTACAGGACCCTCG -3′
- *H3-4* FOR 5′-GTGTCATCCATGCCAAACGG-3′
- *H3-4* REV 5′-GTGGCGAGATAGCCCTCCTA-3′
- *ACTB* FOR 5′-TCCCTGGAGAAGAGCTACG-3′
- *ACTB* REV 5′-GTAGTTTCGTGGATGCCACA-3′

Animal care

As the animal model of amyloid pathology, we used APP/PS1 mice, a double transgenic line, expressing a chimeric mouse/human APP (Mo/HuAPPswe) and human mutated Presenilin 1 (PS1-dE9).[20,22] Primary hippocampal neuronal cultures were prepared from embryonic day 18–19 (E18–E19) Sprague-Dawley rat embryos, obtained from timed-pregnant females purchased from Charles River Laboratories (Calco, Italy). All procedures involving animals were approved by the Italian Ministry of Health and were conducted in accordance with the ethical standards of the Institutional Animal Care and Use Committee of the University of Milan (Italian Ministry of Health permit #5247B.N.YCK/2018 and #284/2019). Mice were housed two to four per cage with *ad libitum* access to food and water, in a controlled environment with a 12-h light and 12-h dark cycle and a controlled temperature of 22°C.

Surgical procedures

Four-month-old APP/PS1 or WT mice were anesthetized using a mix of isoflurane (2%) and oxygen (1.5%) and positioned in a stereotaxic frame (Stoelting) linked to a digital micromanipulator. Microinjection was performed in the hippocampus with a viral vector to overexpress CAP2 levels or a control vector, using the following AAV vectors (serotype 9) purchased from the AAV vector unit (International Center for Genetic Engineering and Biotechnology (ICGEB), Trieste, Italy):

- AAV9-hSyn-eGFP:T2A:mycCAP2
- AAV9-hSyn-eGFP

The coordinates for the stereotaxic injection were confirmed using a mouse brain atlas[50] to inject the viral vectors into the whole hippocampus: AP: −2.0 mm; ML: ±1.5 mm; DV: −1.8, −1.3 mm. The volume of AAV injection was 400 nL (200 nL at DV: −1.8 and 200 nL at DV: −1.3) per hemisphere. The AAV9-hSyn-eGFP:T2A:mycCAP2 vector had a titer of 1.0×10^{14} genome copies per mL (GC/mL), corresponding to a dose of approximately 4.0×10^{10} GC per site. The control vector had a titer of 1.4×10^{14} GC/mL, delivering approximately 5.6×10^{10} GC per site. The virus was infused using a 10-μL Hamilton syringe. After infusion, the pipette was kept in place for 5 min. After the virus injection, the mice were allowed 8 weeks to recover and for the viral vector to adequately express. At the age of 6 months, mice were euthanized for analysis. Additional experimental groups, including mice unilaterally injected and euthanized 4 weeks post-injection for validation of CAP2 overexpression efficiency, as well as animals analyzed for behavioral outcomes at 9 months of age, are described in the corresponding supplemental figure legends.

Tissue-slice preparation and IHC

Anesthetized mice were transcardially perfused with 40 mL of phosphate-buffered saline (PBS 1X, pH 7.2–7.6) followed by cold paraformaldehyde (PFA, 4% in PBS 1X). The brain was removed and post-fixed in 4% PFA in PBS 1X for 24 h, then cryoprotected using a 30% sucrose solution for 24 h. The samples were frozen and 30-μm-thick coronal slices were obtained using a cryostat (Thermo Fisher Scientific). Tissue sections of the dorsal hippocampus were extensively washed in PBS1X and then permeabilized using methanol (pre-chilled at −20°C) for 10 min at room temperature (RT). After permeabilization, brain slices were incubated in blocking solution (PBS 1X; 10% normal goat serum [NGS]) for 1 h and incubated with the appropriate primary antibodies in PBS 1X supplemented with 3% NGS overnight at 4°C. The following day, the appropriate Alexa Fluor-conjugated secondary antibodies, in PBS 1X with 3% NGS, were applied for 1 h at RT followed by nuclei staining with the fluorescent dye 4′,6-diamidino-2-phenylindole (DAPI; 1:50,000 in PBS 1X; Thermo Fisher Scientific).

Spine morphology

For the *ex vivo* analysis of dendritic spine morphology, DiI (Invitrogen) was used to label neurons. The DiI labeling procedure was performed as previously described.[51] Solid DiI crystals were applied to 2-mm coronal sections with a thin needle by gently touching the region of interest. The slices were prepared from brains previously transcardially fixed with 1.5% PFA in 0.1 M phosphate buffer (PB). The DiI was left to diffuse for 24 h in the dark at RT, then slices were post-fixed with 4% PFA in PB 0.1 M for 45 min at 4°C. Coronal sections of 150 μm were obtained using a vibratome, with the first section discarded. Slices were then mounted on glass slides (VWR) with Fluoroshield (Sigma-Aldrich) for confocal imaging.

Neuronal culture preparation, transfection, and treatments

Primary neurons were obtained from the rat hippocampus at E18–19 as previously described.[20] Neuronal cultures were transfected at DIV10 using with the calcium-phosphate coprecipitation method. The plasmids used for each experiment are reported in the figure legends. All the treatments were performed at DIV16 or DIV17 using the protocols described below. The $A\beta_{1\text{-}42}$ peptide and the control sequence $A\beta_{42\text{-}1}$ were purchased from Bachem (Switzerland) and prepared as previously described.[31] Briefly, the peptides were resuspended in 1,1,1,3,3,3-hexafluoro-2-propanol (HFIP; Sigma) at 1 mM

concentration. The solution was aliquoted before the removal of HFIP. Oligomers were obtained by resuspending the preparation in DMSO at 5 mM final concentration, and then further diluted in Neurobasal medium without Phenol red (final concentration 100 μM). Rat primary hippocampal neurons were exposed to either oA$\beta_{1\text{-}42}$ or A$\beta_{42\text{-}1}$ at a concentration of 500 nM in Neurobasal medium supplemented with B27, where the cells were grown. After either 30 min or 24 h of treatment, hippocampal neurons were collected for biochemical or imaging assays. For ATP depletion treatment, the medium was removed and replaced with ATP depletion medium for 30 min (10 mM sodium azide, 6 mM 2-deoxyglucose) as previously described.[5] The treatment was applied in artificial cerebrospinal fluid (ACSF; 125 mM NaCl, 2.5 mM KCl, 1 mM $MgCl_2$, 2 mM $CaCl_2$, 33 mM D-glucose, and 25 mM HEPES; pH 7.4). After 30 min of treatment, hippocampal neurons were processed for imaging analysis.

TIF synaptic membrane purification

TIF, a fraction highly enriched in all categories of postsynaptic density proteins, was obtained from rat primary hippocampal neurons and APP/PS1 or WT hippocampal tissue. The samples were lysed at 4°C in an ice-cold buffer containing 0.32 M sucrose, 1 mM HEPES, 1 mM NaF, 0.1 mM PMSF, and 1 mM $MgCl_2$, in the presence of protease inhibitors (Complete, Roche Diagnostics GmbH) and phosphatase inhibitors (PhosSTOP, Roche Diagnostics GmbH), to obtain the total homogenate. To purify postsynaptic TIFs, the homogenates were centrifuged at 13,000 × *g* for 15 min at 4°C. The pellet was resuspended in an extraction buffer containing 0.5% Triton X-100, 150 mM KCl, and Complete, incubated on ice for 15 min and centrifuged at 100,000 × *g* for 1 h at 4°C. The resulting TIF pellet was dissolved in 20 mM HEPES with Complete, using a glass-glass homogenizer. The protein content of the samples was quantified using the Bio-Rad protein assay reagent (Hercules, CA, USA) and equivalent amounts of proteins were loaded in each lane for WB analysis.

Co-immunoprecipitation assay

Co-immunoprecipitation assays were performed on hippocampal TIFs obtained from APP/PS1 mice injected with AAV9-hSyn-eGFP (AAV-GFP) or AAV9-hSyn-eGFP:T2A:mycCAP2 (AAV-mycCAP2). For samples from AAV-mycCAP2-injected animals, aliquots of 25 μg TIF were incubated with an antibody against cofilin overnight at 4°C in a final volume of 200 μL of RIA buffer (200 mM NaCl, 10 mM ethylene-diaminetetra-acetic acid [EDTA], 10 mM Na_2HPO_4, 0.5% NP-40, 0.1% sodium dodecyl sulfate [SDS]). For samples derived from GFP-injected mice, 50 μg TIF in a final volume of 500 μL of RIA buffer was used. Forty microliters of SureBeads Protein A Magnetic Beads (Bio-Rad) were added to each sample to precipitate the immunocomplex. After three washes with RIA buffer, the beads were collected by centrifugation and then resuspended in sample buffer without β-mercaptoethanol. The samples were heated for 3 min and loaded onto SDS-PAGE to detect CAP2 dimers and monomers. The precipitated immunocomplex was revealed by anti-cofilin and anti-CAP2 antibody and the ratio between the dimeric and monomeric form of CAP2 was evaluated.

Western blot

The proteins were separated on a denaturing sodium dodecyl sulfate-polyacrylamide gel electrophoresis (SDS-PAGE) followed by WB. Ten to 15 μg of proteins were separated on 7% or 12% SDS-PAGE (depending on the molecular weight of the indicated proteins) and transferred onto a nitrocellulose membrane. In order to detect CAP2 dimers and monomers, the protein samples were prepared in Laemmli buffer without β-mercaptoethanol and heated for 5 min before loading onto SDS-PAGE. The membranes were then incubated with the specific primary antibody in blocking solution (I-block, Tris-buffered saline [TBS] 1X, 20% Tween 20) overnight at 4 C°. The following day, after three washes with TBS and tween 20 (TBS + tween 20 0.1%), they were incubated with a corresponding horseradish peroxidase (HRP)-conjugated secondary antibody in blocking solution for 1 h at RT. The proteins were detected by chemiluminescence using Clarity Western ECL substrate reagent (Bio-Rad cat. number 170–5061) and acquired with a ChemiDoc instrument (Bio-Rad).

In situ PLA

Primary hippocampal cultures were treated at DIV 16 and then fixed with 4% PFA in PBS + 4% sucrose for 10 min at RT. Coverslips were then washed three times with PBS and permeabilized with Triton X-100 0.1% in PBS for 15 min. Subsequently, the PLA was performed. After incubation with the blocking solution of the PLA kit (Duolink PLA Technology), cells were incubated overnight with goat monoclonal anti-CAP2 antibody (1:100; Santa Cruz Biotechnology) and rabbit polyclonal anti-cofilin antibody (1:100; Cell Signaling) overnight at 4°C in a humidified chamber. According to the manufacturer's instructions, after washing with wash buffer A, cells were incubated for 1 h at 37°C with secondary probes anti-goat Plus and anti-rabbit Minus. Coverslips were then washed twice with buffer A and incubated with the ligation solution supplemented with ligase for 30 min at 37°C, before washing again with buffer A. The oligonucleotides of the bound probes were amplified by a DNA polymerase in the amplification buffer for 90 min at 37°C in a humid dark chamber. Cells were next washed with Wash Buffer B and then, to stain MAP2 or mycCAP2, the immunocytochemistry (ICC) protocol was performed. Cells were mounted on slides using Fluoromount TM Aqueous Mounting Medium (Sigma-Aldrich).

Immunofluorescence

Hippocampal neurons were fixed for 10 min at RT in 4% PFA +4% sucrose in PBS. Coverslips were then washed several times with PBS and permeabilized with 0.1% Triton X-100 in PBS for 15 min at RT. ICC labeling of cofilin-actin rods was performed as previously described.[30] Briefly, cells were fixed for 45 min at RT in 4% PFA + 4% sucrose in PBS. After washing in PBS, cells were permeabilized using methanol (prechilled at −20°C) for 3 min at RT. Coverslips were then blocked for 1 h at RT with 5% bovine serum albumin (BSA) in PBS and incubated with primary antibodies in 1% BSA-PBS overnight at 4°C in a humid chamber. After washing with PBS, the cells were incubated with the appropriate secondary antibodies in 1% BSA-PBS for 1 h at RT. The incubation was followed

Please cite this article in press as: Stringhi et al., Cyclase-associated protein 2 gene delivery: A potential multi-target approach for preventing synaptic failure in Alzheimer's disease, Molecular Therapy (2025), https://doi.org/10.1016/j.ymthe.2025.12.023

by washing with PBS and mounting on glass slides using Fluoroshield mounting medium (Sigma-Aldrich).

Confocal microscopy

Images were acquired with a Zeiss confocal laser scanning microscope LSM900 as a z stack series, using an LD C-Apochromat 40×/NA 1.1 W objective. For dendritic spine density analysis in primary hippocampal neurons, a zoom of 2× was employed. The images for *ex vivo* spine morphology analysis were obtained using a Nikon A1R confocal microscope as a z stack series with a Plan Apo 60×/NA 1.42 oil immersion objective performing sequential acquisition at a digital resolution of 1,024 × 1,024 pixels. SIM Multichannel images were acquired using a Nikon Structured Illumination super-resolution microscope using a 100 × 1.4 NA objective and reconstructed using Nikon Elements software. IHC images were acquired using an EC Plan-Neofluar 20×/NA 0.50 objective. Three-dimensional colocalization experiments were conducted from the z stack series taken in super-resolution modality using an LSM900 confocal microscope with the Airyscan detector (Carl Zeiss) and equipped with a Plan Apo 63×/NA 1.40 oil immersion objective.

Three-dimensional colocalization analysis

Three-dimensional images were reconstructed and analyzed using Arivis Vision4D v.4.00 (Arivis a Zeiss company; http://www.arivis.com). Cofilin-actin rods were detected using the intensity threshold segmenter, based on cofilin signal intensity. The blob finder segmenter was used to detect CAP2 dots. Compartment operation analysis was performed to study colocalization between cofilin-actin rods and CAP2 signal in order to detect CAP2 voxels located inside rods. Only CAP2 voxels that were 100% overlapping with cofilin rod signal were taken into consideration for the analysis. For each rod, parameters such as volume and sphericity were evaluated and used for comparison between CAP2-containing and CAP2-negative actin rods.

Quantification of data

WB images were quantified using computer-assisted imaging (Image Lab 4.0 software; Bio-Rad). Quantities of proteins were expressed as relative optical density (OD) measurements and normalized to Tubulin, Actin, Calnexin, or GAPDH, and then expressed as a percentage of the control mean. For imaging analysis, for each condition, a minimum of eight neurons were randomly chosen from at least two independent preparations. z stack images were processed and analyzed using Fiji software (US National Institutes of Health). Cofilin localization in spines was analyzed assuming that the spine volume and the amount of fusion protein were proportional to the integrated intensity of the GFP signal.[11] The analysis of PLA experiments and dendritic spine density was performed using Fiji software and the number of clusters or dendritic spines was normalized to the total dendritic length. Spine density and morphology analysis were performed using Fiji software, and spine length, head width, and neck width were assessed for each spine using the straight-line function. Spines were classified into three types (thin, stubby, or mushroom) based on length, neck, and head width. To minimize the possibility of bias, the quantification of actin rods was performed using automatic analysis. Briefly, we set up an automated threshold to remove the background signal deriving from physiological levels of cofilin by calculating a fixed value for each image based on the histogram of gray values distribution. To do this, we used the following formula:

$$Threshold = (3 \times StdDev) + peak\ value \quad \text{(Equation 1)}$$

Only the pixels in which cofilin immunoreactivity intensity exceeded this value were considered. For the analysis, only particles with an area >0.5 μm^2 were measured. For brain sections, the analyzed fields were taken at five pre-determined locations on three sections from each animal. Cofilin rods were defined as objects with a major axis longer than 2 μm, a minor axis shorter than 1.5 μm, and an aspect ratio larger than 2, as previously described.[52] β-amyloid plaques in the hippocampus were quantified using Fiji software. For each section, plaques were manually delineated in the hippocampal region to measure both plaque number and total plaque area. Values were normalized to the total hippocampal area analyzed in each section. Quantifications were performed on comparable coronal sections across animals.

Novel object recognition and spatial displacement task

The methods used to perform novel object recognition and spatial displacement tasks were adapted from a previous protocol.[53] Both of the tests consist of an acquisition (10 min) and a recognition step (10 min), executed with a 24-h interval. Mice were tested in a standard open field arena (UgoBasile, 44 × 44 cm) with black PVC walls. All animals were habituated to the open field arena for 1 h the day before testing. Objects constructed from Duplo (Lego) blocks were used as stimuli, with care taken to alternate their shape, color, and size. A digital camera (Imaging Source, DMK 22AUC03 monochrome) was mounted above the open field apparatus to record the test. A behavioral tracking system (Anymaze 6.0, Stoelting, UK) was used for scoring the time spent in the different zones of the apparatus. To express discrimination between the objects, the percentage of time spent exploring the familiar, novel, and displaced objects was calculated and compared with the total navigation time, which was defined as the animal directing its nose toward an object at a distance of at least 2 cm. Animals that failed to complete a minimum of 10 s of exploration in the test phase were excluded from the analysis. During the NORT, the acquisition phase was performed by placing two identical objects close to the corners of one wall in the arena (10 cm from the walls). On the test day, one of the two objects was replaced with a novel object. In the spatial displacement task, we measured the ability of mice to recognize the altered position of an object during the test compared with the acquisition phase. Therefore, in the acquisition phase, two identical objects were placed near the corners of one wall in the arena, whereas, in the test, one object was displaced to the corner adjacent to its original position, such that the two objects were diagonal from each other.

Barnes maze and reversal learning test

The Barnes maze is a hippocampal-dependent task where animals learn the relationship between distal cues in the surrounding

Please cite this article in press as: Stringhi et al., Cyclase-associated protein 2 gene delivery: A potential multi-target approach for preventing synaptic failure in Alzheimer's disease, Molecular Therapy (2025), https://doi.org/10.1016/j.ymthe.2025.12.023

environment and a fixed escape location.[54] The maze is a white circular platform (UgoBasile) with a diameter of 100 cm, elevated at 60 cm from the floor with 20 equally spaced holes along the perimeter (each hole has a diameter of 5 cm) located 2 cm from the platform's edge. Visual cues were located on the walls of the room. A black plexiglass escape box (114 × 114 × 50 mm) was mounted underneath one hole, while the remaining 19 holes were left empty. From above, the platform was illuminated by a bright light of ∼650 lx, with both bright light and open spaces serving as motivating factors to induce escape behavior. On the platform sides, two incandescent lamps were placed to provide dim light to conduct the experiment when the bright illumination was turned off. The experimental design was adapted from previous protocols.[55,56] The day before the test, a habituation phase consisting of three sessions at 15-min intervals was carried out without bright illumination. At the start of each session, mice were placed under a start box located in the center of the platform for 1 min. The box was then removed, and the animals were allowed to explore the arena for 30 s. After this time, the mice were guided to the escape box by the experimenter. Mice were kept in the escape box for 1 min. During the test phase, mice were positioned in the start box for 1 min with the bright illumination turned off. After time had elapsed, the illumination was turned on, the chamber was lifted, and the mouse was free to explore the maze. The session was concluded when the mouse entered the escape box, or after 3 min. When the mouse entered the escape box, the lights were turned off, and the mouse was left in the dark for 1 min. If the mouse did not find the escape box within 3 min, the experimenter gently guided the mouse to the escape box. The test involved three daily trials at intervals of 15 min, spread over 4 days. The location of the escape box remained the same for a given mouse but was randomized across mice. Reversal learning was performed 2 weeks after the final acquisition phase (day 4) by moving the escape box to a new position opposite to the original (i.e., 180° from its previous location). Mice were then subjected to three consecutive trials to establish the new position of the escape hole, using the same procedure as described above. A digital camera (Imaging Source, DMK 22AUC03 monochrome) was positioned above the circular apparatus to record the test, and a behavioral tracking system (Anymaze 6.0, Stoelting, UK) was used to measure the amount of time taken to reach the escape box (latency to escape) and to evaluate the overall efficiency of spatial navigation exhibited (path efficiency). An unbiased machine-learning algorithm, called BUNS, was used to classify and calculate specific spatial strategies used in the Barnes maze during reversal learning. BUNS allows the identification of specific strategies such as random, serial, focused search, long correction, corrected, and direct, based on Anymaze behavioral tracking. In addition, BUNS automatically assigns a specific score, called the cognitive score, to numerically evaluate the success, in terms of spatial navigation, of each of these strategies.[57]

Antibodies list

The following primary antibodies (Ab) were used: goat anti-CAP2 (PLA 1:100, Santa Cruz Biotechnology, #SC-167378), rabbit anti-CAP2 (WB 1:1,000, ICC 1:400, IHC 1:400, Proteintech, #15865-1-AP), mouse anti-CAP2 (WB 1:2,000, PLA 1:100, Proteintech, #67412-1-Ig), mouse anti-CAP2 (ICC 1:200, Santa Cruz Biotechnology, #SC-377471), mouse anti-actin (WB 1:4,000, Proteintech, #66009-1-Ig), mouse anti-Tubulin (WB 1:10,000, Sigma-Aldrich, #T9026), mouse anti-Myc (9E10) (WB 1:2,000, ICC 1:400, IHC 1:400, Roche, #11667149001), mouse anti-GFP (JL-8) (WB 1:2,000, Clontech, #632381), rabbit anti-cofilin (WB 1:1,000, PLA 1:100, ICC 1:600, IHC 1:600, Cell Signaling, #5175), guinea pig anti-MAP2 (ICC 1:300, Synaptic Systems, #188004), rabbit anti-GADPH (WB 1:1000, Santa Cruz Biotechnology, #SC-25778), rabbit anti-pCofilin (WB 1:1,000, Cell Signaling, #33135), rabbit anti-Calnexin (WB 1:1,000, Enzo Life Sciences, #ADI-SPA-860), mouse anti-β-amyloid 6E10 (IHC 1:500, BioLegend, # 803001), rabbit anti-CREB (WB 1:1,000, Cell Signaling, #9197), rabbit anti-pCREB (WB 1:1,000, Cell Signaling, #9198), rabbit anti-Tau (WB 1:1,000, DAKO, #A0024), rabbit anti-p-Tau (WB 1:1,000, Cell Signaling, #12885). The Alexa Fluor dye secondary antibodies used (goat anti-mouse-Alexa405, goat anti-mouse-Alexa488, goat anti-mouse-Alexa555, goat anti-rabbit-Alexa488, goat anti-rabbit-Alexa555, goat anti-mouse-Alexa647 and goat anti-guinea pig-Alexa647) were purchased from Thermo Fisher Scientific. The peroxidase-conjugated secondary antibodies were purchased from Bio-Rad.

Statistical analysis

Multiple regression models were applied to the *in vivo* and *in vitro* imaging experiments to estimate beta coefficients, corresponding standard errors (SEs) and *p* values of the treatment effect. In principle, mixed-effects models[58] should be specified for each experiment and outcome variable of interest within the experiment to account for the hierarchical structure of the experimental designs.[47] In the *in vitro* imaging analyses, actin rods belonged to neurons and neurons belonged to cultures in experiments presented in Figure 4D; dendritic spines belonged to neurons and neurons belonged to cultures in experiments shown in Figure S5B; neurons belonged to cultures in experiments presented in Figures 5D, 5E, 6B–6D, and S4A. However, for the culture hierarchical level, we observed at most four cultures per experiment; as modern theory on mixed-effects models suggests that the estimation of the variance of random-effects terms might be difficult when fewer than five categories are available for the hierarchical level, we avoided specifying a random effect for culture and consistently treated it as a fixed effect across all the experiments under investigation. For the neuron hierarchical level (available from experiments in Figures 4D and S5B), the five categories were reached for the most part, and neuron was then generally treated as a random intercept within a mixed-effects model, including culture and treatment as fixed-effects, as far as the model converged (Figure 4D, outcome actin rod volume and sphericity; Figure S5B). In the remaining cases, we fitted a fixed-effects model including treatment and culture (as well as neuron when convergence issues arose) as independent variables by using the robust linear regression method with the MM estimator to account for the violation of ordinary least squares assumptions.

In addition, the *in vivo* imaging analyses were carried out by considering the following hierarchical structure in spine morphology: spine

belonged to dendrites, dendrites were visualized across multiple images, and multiple images were obtained from each animal. When the outcome variable under consideration was spine density, the experimental unit was dendritic spine and the available hierarchical levels were images and animals; when the outcome variable was spine length, width, or type, the experimental unit was the spine, and the available hierarchical levels were dendrites, images, and animals. All *in vivo* spine morphology analyses were restricted to images with a quality score >2.6 as determined by the researcher who performed the blind analysis.

Among mixed-effects models, most were linear mixed-effects (LMM) models; generalized LMM models with a logit link function and binomial family were fitted for the type outcome variable for the *in vivo* spine morphology experiments; in these analyses, the outcome variable was treated in the following three ways: (1) stubby spines (reference category) and mushroom spines; (2) thin spines (reference category) and mushroom spines; and (3) non-mushroom spines (reference category including filopodia, thin, and stubby spines) and mushroom spines. For fitting mixed-effects models, restricted maximum-likelihood (REML) estimates were used, as they provide more reliable estimates of variance components. To test model assumptions, we plotted residuals vs. fitted values for each model; when outliers were detected, they were checked at the experimental level.

Hypothesis testing on the significance of single parameters (Wald's test) was performed within the robust linear or the LMM with the robust F or the Student's *t* distribution, respectively; a Gaussian distribution was adopted for the generalized LMM models. The (eventually robust) F statistics from the ANOVA analysis provided information on the overall significance of each independent variable entered in the models. When suitable, contrasts of interest were extracted to calculate the estimated mean differences and corresponding SEs between pairs of available experimental arms under examination in each model. Finally, the chi-square test of independence was used to assess the presence of an association between spine type and genetic treatment.

Regarding behavioral tests, analysis of strategies (Figure 2D) were similarly analyzed by using mixed-effects models where treatment and the trial number were entered as fixed-effects terms, and the mouse ID was entered as the random-effect term; the interaction between treatment and trial number was tested by using the likelihood ratio test on maximum-likelihood refitted models including vs. excluding the interaction term; however, the corresponding p value exceeded 0.05 and was therefore omitted from the final model. The analyses of behavioral experiments were restricted to those behaviors exhibited by at least six mice in at least one of the two arms, no matter the trial (i.e., a random or a serial behavior).

Calculations were carried out using the open-source statistical computing environment R (R Core Team, 2023) with its libraries lme4,[59] lmerTest,[60] and emmeans,[61] for the above-reported experiments. For all other experiments, comparisons between groups were performed using the following tests as appropriate: two-tailed unpaired Student's *t* test, Mann-Whitney test, Wilcoxon test, nested *t* test, or two-way ANOVA. Throughout the manuscript, values were reported as mean ± SE. The type of parametric test used for each experiment and the corresponding p values, as well as the numbers of neurons and mice used, are reported in the figure legends. Significance was assumed if $p < 0.05$. Calculations were performed using Prism 9 (GraphPad, La Jolla, CA, USA).

DATA AVAILABILITY

All data generated or analyzed during this study are included in this published article and its supplemental information files. The datasets used and/or analyzed during the current study are available from the corresponding author on reasonable request.

ACKNOWLEDGMENTS

This project has received funding from the Italian Ministry of Research and University (MUR) (PRIN202039WMFP, PRIN2022 PNRR P2022R2E8N to E.M., PRIN 20202THZAW and PRIN2022 PNRR P2022TKN8C, Fondo Italiano per la Scienza FIS00000560 - Stone, PNRR, Missione 4 – Componente 2– Investimento 1.3, finanziato dall'Unione europea – NextGenerationEU "Fascination" to M.D.L.), from the Giovanni Armenise-Harvard Foundation and Airalzh ONLUS (2023 Armenise Harvard-AIRALZH Mid-Career Award in Neurodegenerative Diseases - AHA MCA - to E.M.), from the Italian Ministry of Enterprises and Made in Italy (PNRR - NextGenerationEU funding, "SEED for Innovation Patent 2.0" program, project TT_MIN23_SEED4IP2.0_07 to E.M.), from Piano di Sostegno alla Ricerca (PSR), Università degli Studi di Milano (PSR2022_DIP_022_AZIONE_A_SPELU, PSR2025_SPELU and PSR2023_SPELU to S.P.), EMBO Scientific Exchange Grant (number 10360) and The Company of Biologists Travel Grant (number JCSTF23051053) to R.S.

This work was also supported by MUR Progetto Eccellenza (2022–2027) to the Dipartimento di Scienze Farmacologiche e Biomolecolari "Rodolfo Paoletti," Università degli Studi di Milano.

We thank Annalisa Longhi for her technical assistance and Elena Avaldi, Federica Mascellani, Adriana Schneider, and Melissa Torone for their excellent practical work. Part of this work was carried out at NOLIMITS, an advanced imaging facility established by the Università degli Studi di Milano. The brain tissues were obtained from the Netherlands Brain Bank, Netherlands Institute for Neuroscience, Amsterdam. The graphical abstract was created with BioRender.com.

AUTHOR CONTRIBUTIONS

Conceptualization, R.S., S.P., M.D.L., and E.M. Investigation, R.S., S.P., L.D., F.L.G., E.Z., L.T., C.M., and L.V. Software, M.A. Formal analysis, R.S, S.P., C.M., M.C.S., and V.E. Supervision, D.S., V.E., M.D.L., and E.M. Writing – Original Draft, R.S., S.P., M.D.L., and E.M. Writing – Review & Editing, F.G., D.S., and V.E. Funding acquisition, S.P., R.S., M.D.L., and E.M.

DECLARATION OF INTERESTS

The authors declare no competing interests.

DECLARATION OF GENERATIVE AI AND AI-ASSISTED TECHNOLOGIES IN THE WRITING PROCESS

During the preparation of this work, the authors used ChatGPT to improve language and readability. After using this tool, they reviewed and edited the content as needed and took full responsibility for the publication's content.

SUPPLEMENTAL INFORMATION

Supplemental information can be found online at https://doi.org/10.1016/j.ymthe.2025.12.023.

REFERENCES

1. Gentile, J.E., Carrizales, M.G., and Koleske, A.J. (2022). Control of synapse structure and function by actin and its regulators. Cells *11*, 603. https://doi.org/10.3390/cells11040603.
2. Pelucchi, S., Stringhi, R., and Marcello, E. (2020). Dendritic spines in Alzheimer's disease: how the actin cytoskeleton contributes to synaptic failure. Int. J. Mol. Sci. *21*, 908. https://doi.org/10.3390/ijms21030908.
3. Kang, D.E., and Woo, J.A. (2019). Cofilin, a master node regulating cytoskeletal pathogenesis in Alzheimer's disease. J. Alzheimers Dis. *72*, S131–S144. https://doi.org/10.3233/jad-190585.
4. Bamburg, J.R., Bernstein, B.W., Davis, R.C., Flynn, K.C., Goldsbury, C., Jensen, J.R., Maloney, M.T., Marsden, I.T., Minamide, L.S., Pak, C.W., et al. (2010). ADF/cofilin-actin rods in neurodegenerative diseases. Curr. Alzheimer Res. *7*, 241–250. https://doi.org/10.2174/156720510791050902.
5. Minamide, L.S., Striegl, A.M., Boyle, J.A., Meberg, P.J., and Bamburg, J.R. (2000). Neurodegenerative stimuli induce persistent ADF/cofilin–actin rods that disrupt distal neurite function. Nat. Cell Biol. *2*, 628–636. https://doi.org/10.1038/35023579.
6. Davis, R.C., Marsden, I.T., Maloney, M.T., Minamide, L.S., Podlisny, M., Selkoe, D.J., and Bamburg, J.R. (2011). Amyloid beta dimers/trimers potently induce cofilin-actin rods that are inhibited by maintaining cofilin-phosphorylation. Mol. Neurodegener. *6*, 10. https://doi.org/10.1186/1750-1326-6-10.
7. Maloney, M.T., and Bamburg, J.R. (2007). Cofilin-mediated neurodegeneration in Alzheimer's disease and other amyloidopathies. Mol. Neurobiol. *35*, 21–44. https://doi.org/10.1007/bf02700622.
8. Walsh, K.P., Minamide, L.S., Kane, S.J., Shaw, A.E., Brown, D.R., Pulford, B., Zabel, M.D., Lambeth, J.D., Kuhn, T.B., and Bamburg, J.R. (2014). Amyloid-β and proinflammatory cytokines utilize a prion protein-dependent pathway to activate NADPH oxidase and induce cofilin-actin rods in hippocampal neurons. PLoS One *9*, e95995. https://doi.org/10.1371/journal.pone.0095995.
9. Borovac, J., Bosch, M., and Okamoto, K. (2018). Regulation of actin dynamics during structural plasticity of dendritic spines: signaling messengers and actin-binding proteins. Mol. Cell. Neurosci. *91*, 122–130. https://doi.org/10.1016/j.mcn.2018.07.001.
10. Rust, M.B., Gurniak, C.B., Renner, M., Vara, H., Morando, L., Görlich, A., Sassoè-Pognetto, M., Banchaabouchi, M.A., Giustetto, M., Triller, A., et al. (2010). Learning, AMPA receptor mobility and synaptic plasticity depend on n-cofilin-mediated actin dynamics. EMBO J. *29*, 1889–1902. https://doi.org/10.1038/emboj.2010.72.
11. Bosch, M., Castro, J., Saneyoshi, T., Matsuno, H., Sur, M., and Hayashi, Y. (2014). Structural and molecular remodeling of dendritic spine substructures during long-term potentiation. Neuron *82*, 444–459. https://doi.org/10.1016/j.neuron.2014.03.021.
12. Calabrese, B., Saffin, J.M., and Halpain, S. (2014). Activity-dependent dendritic spine shrinkage and growth involve downregulation of cofilin via distinct mechanisms. PLoS One *9*, e94787. https://doi.org/10.1371/journal.pone.0094787.
13. Normoyle, K.P.M., and Brieher, W.M. (2012). Cyclase-associated protein (CAP) acts directly on F-actin to accelerate cofilin-mediated actin severing across the range of physiological pH. J. Biol. Chem. *287*, 35722–35732. https://doi.org/10.1074/jbc.m112.396051.
14. Chaudhry, F., Breitsprecher, D., Little, K., Sharov, G., Sokolova, O., and Goode, B.L. (2013). Srv2/cyclase-associated protein forms hexameric shurikens that directly catalyze actin filament severing by cofilin. Mol. Biol. Cell *24*, 31–41. https://doi.org/10.1091/mbc.e12-08-0589.
15. Kodera, N., Abe, H., Nguyen, P.D.N., and Ono, S. (2021). Native cyclase-associated protein and actin from Xenopus laevis oocytes form a unique 4:4 complex with a tripartite structure. J. Biol. Chem. *296*, 100649. https://doi.org/10.1016/j.jbc.2021.100649.
16. Kotila, T., Wioland, H., Enkavi, G., Kogan, K., Vattulainen, I., Jégou, A., Romet-Lemonne, G., and Lappalainen, P. (2019). Mechanism of synergistic actin filament pointed end depolymerization by cyclase-associated protein and cofilin. Nat. Commun. *10*, 5320. https://doi.org/10.1038/s41467-019-13213-2.
17. Shekhar, S., Chung, J., Kondev, J., Gelles, J., and Goode, B.L. (2019). Synergy between cyclase-associated protein and cofilin accelerates actin filament depolymerization by two orders of magnitude. Nat. Commun. *10*, 5319. https://doi.org/10.1038/s41467-019-13268-1.
18. Alimov, N., Hoeprich, G.J., Padrick, S.B., and Goode, B.L. (2023). Cyclase-associated protein interacts with actin filament barbed ends to promote depolymerization and formin displacement. J. Biol. Chem. *299*, 105367. https://doi.org/10.1016/j.jbc.2023.105367.
19. Peche, V., Shekar, S., Leichter, M., Korte, H., Schröder, R., Schleicher, M., Holak, T.A., Clemen, C.S., Ramanath-Y, B., Pfitzer, G., et al. (2007). CAP2, cyclase-associated protein 2, is a dual compartment protein. Cell. Mol. Life Sci. *64*, 2702–2715. https://doi.org/10.1007/s00018-007-7316-3.
20. Pelucchi, S., Vandermeulen, L., Pizzamiglio, L., Aksan, B., Yan, J., Konietzny, A., Bonomi, E., Borroni, B., Padovani, A., Rust, M.B., et al. (2020). Cyclase-associated protein 2 dimerization regulates cofilin in synaptic plasticity and Alzheimer's disease. Brain Commun. *2*, fcaa086. https://doi.org/10.1093/braincomms/fcaa086.
21. Padovani, A., Pilotto, A., Pelucchi, S., D'Andrea, L., Stringhi, R., Gorla, F., Aksan, B., Caratozzolo, S., Benussi, A., Galli, A., et al. (2025). Cerebrospinal fluid cyclase-associated protein 2 is increased in Alzheimer's disease and correlates with tau pathology. Transl. Neurodegener. *14*, 1. https://doi.org/10.1186/s40035-024-00462-5.
22. Musardo, S., Therin, S., Pelucchi, S., D'Andrea, L., Stringhi, R., Ribeiro, A., Manca, A., Balducci, C., Pagano, J., Sala, C., et al. (2022). The development of ADAM10 endocytosis inhibitors for the treatment of Alzheimer's disease. Mol. Ther. *30*, 2474–2490. https://doi.org/10.1016/j.ymthe.2022.03.024.
23. Askenazi, M., Kavanagh, T., Pires, G., Ueberheide, B., Wisniewski, T., and Drummond, E. (2023). Compilation of reported protein changes in the brain in Alzheimer's disease. Nat. Commun. *14*, 4466. https://doi.org/10.1038/s41467-023-40208-x.
24. Trinchese, F., Liu, S., Battaglia, F., Walter, S., Mathews, P.M., and Arancio, O. (2004). Progressive age-related development of Alzheimer-like pathology in APP/PS1 mice. Ann. Neurol. *55*, 801–814. https://doi.org/10.1002/ana.20101.
25. Aschauer, D.F., Kreuz, S., and Rumpel, S. (2013). Analysis of transduction efficiency, tropism and axonal transport of AAV serotypes 1, 2, 5, 6, 8 and 9 in the mouse brain. PLoS One *8*, e76310. https://doi.org/10.1371/journal.pone.0076310.
26. Barco, A., Alarcon, J.M., and Kandel, E.R. (2002). Expression of constitutively active CREB protein facilitates the late phase of long-term potentiation by enhancing synaptic capture. Cell *108*, 689–703. https://doi.org/10.1016/s0092-8674(02)00657-8.
27. Saunders, T.S., Pozzolo, F.E., Heslegrave, A., King, D., McGeachan, R.I., Spires-Jones, M.P., Harris, S.E., Ritchie, C., Muniz-Terrera, G., Deary, I.J., et al. (2023). Predictive blood biomarkers and brain changes associated with age-related cognitive decline. Brain Commun. *5*, fcad113. https://doi.org/10.1093/braincomms/fcad113.
28. Zhang, S., Chai, R., Yang, Y.Y., Guo, S.Q., Wang, S., Guo, T., Xu, S.F., Zhang, Y.H., Wang, Z.Y., and Guo, C. (2017). Chronic diabetic states worsen Alzheimer neuropathology and cognitive deficits accompanying disruption of calcium signaling in leptin-deficient APP/PS1 mice. Oncotarget *8*, 43617–43634. https://doi.org/10.18632/oncotarget.17116.
29. Davis, R.C., Maloney, M.T., Minamide, L.S., Flynn, K.C., Stonebraker, M.A., and Bamburg, J.R. (2009). Mapping cofilin-actin rods in stressed hippocampal slices and the role of cdc42 in amyloid-beta-induced rods. J. Alzheimers Dis. *18*, 35–50. https://doi.org/10.3233/jad-2009-1122.
30. Minamide, L.S., Maiti, S., Boyle, J.A., Davis, R.C., Coppinger, J.A., Bao, Y., Huang, T.Y., Yates, J., Bokoch, G.M., and Bamburg, J.R. (2010). Isolation and characterization of cytoplasmic cofilin-actin rods. J. Biol. Chem. *285*, 5450–5460. https://doi.org/10.1074/jbc.M109.063768.
31. Marcello, E., Musardo, S., Vandermeulen, L., Pelucchi, S., Gardoni, F., Santo, N., Antonucci, F., and Di Luca, M. (2019). Amyloid-β oligomers regulate ADAM10 synaptic localization through aberrant plasticity phenomena. Mol. Neurobiol. *56*, 7136–7143. https://doi.org/10.1007/s12035-019-1583-5.
32. Barone, E., Mosser, S., and Fraering, P.C. (2014). Inactivation of brain Cofilin-1 by age, Alzheimer's disease and γ-secretase. Biochim. Biophys. Acta *1842*, 2500–2509. https://doi.org/10.1016/j.bbadis.2014.10.004.
33. Rush, T., Martinez-Hernandez, J., Dollmeyer, M., Frandemiche, M.L., Borel, E., Boisseau, S., Jacquier-Sarlin, M., and Buisson, A. (2018). Synaptotoxicity in Alzheimer's disease involved a dysregulation of actin cytoskeleton dynamics through

Cofilin 1 phosphorylation. J. Neurosci. *38*, 10349–10361. https://doi.org/10.1523/jneurosci.1409-18.2018.

34. Rahman, T., Davies, D.S., Tannenberg, R.K., Fok, S., Shepherd, C., Dodd, P.R., Cullen, K.M., and Goldsbury, C. (2014). Cofilin rods and aggregates concur with tau pathology and the development of Alzheimer's disease. J. Alzheimers Dis. *42*, 1443–1460. https://doi.org/10.3233/jad-140393.

35. Namme, J.N., Bepari, A.K., and Takebayashi, H. (2021). Cofilin signaling in the CNS physiology and neurodegeneration. Int. J. Mol. Sci. *22*, 10727. https://doi.org/10.3390/ijms221910727.

36. Bamburg, J.R., Minamide, L.S., Wiggan, O., Tahtamouni, L.H., and Kuhn, T.B. (2021). Cofilin and actin dynamics: multiple modes of regulation and their impacts in neuronal development and degeneration. Cells *10*, 2726. https://doi.org/10.3390/cells10102726.

37. Uruk, G., Mocanu, E., Shaw, A.E., Bamburg, J.R., and Swanson, R.A. (2024). Cofilactin rod formation mediates inflammation-induced neurite degeneration. Cell Rep. *43*, 113914. https://doi.org/10.1016/j.celrep.2024.113914.

38. Wurz, A.I., Schulz, A.M., O'Bryant, C.T., Sharp, J.F., and Hughes, R.M. (2022). Cytoskeletal dysregulation and neurodegenerative disease: formation, monitoring, and inhibition of cofilin-actin rods. Front. Cell. Neurosci. *16*, 982074. https://doi.org/10.3389/fncel.2022.982074.

39. Kuhn, T.B., Minamide, L.S., Tahtamouni, L.H., Alderfer, S.A., Walsh, K.P., Shaw, A.E., Yanouri, O., Haigler, H.J., Ruff, M.R., and Bamburg, J.R. (2024). Chemokine receptor antagonists prevent and reverse cofilin-actin rod pathology and protect synapses in cultured rodent and human iPSC-derived neurons. Biomedicines *12*, 93. https://doi.org/10.3390/biomedicines12010093.

40. Cichon, J., Sun, C., Chen, B., Jiang, M., Chen, X.A., Sun, Y., Wang, Y., and Chen, G. (2012). Cofilin aggregation blocks intracellular trafficking and induces synaptic loss in hippocampal neurons. J. Biol. Chem. *287*, 3919–3929. https://doi.org/10.1074/jbc.m111.301911.

41. Jang, D.H., Han, J.H., Lee, S.H., Lee, Y.S., Park, H., Lee, S.H., Kim, H., and Kaang, B.K. (2005). Cofilin expression induces cofilin-actin rod formation and disrupts synaptic structure and function in Aplysia synapses. Proc. Natl. Acad. Sci. USA *102*, 16072–16077. https://doi.org/10.1073/pnas.0507675102.

42. Whiteman, I.T., Gervasio, O.L., Cullen, K.M., Guillemin, G.J., Jeong, E.V., Witting, P.K., Antao, S.T., Minamide, L.S., Bamburg, J.R., and Goldsbury, C. (2009). Activated actin-depolymerizing factor/cofilin sequesters phosphorylated microtubule-associated protein during the assembly of Alzheimer-like neuritic cytoskeletal striations. J. Neurosci. *29*, 12994–13005. https://doi.org/10.1523/jneurosci.3531-09.2009.

43. Daly, T., Kepp, K.P., and Imbimbo, B.P. (2024). Are lecanemab and donanemab disease-modifying therapies? Alzheimers Dement. *20*, 6659–6661. https://doi.org/10.1002/alz.14114.

44. Woo, J.A., Zhao, X., Khan, H., Penn, C., Wang, X., Joly-Amado, A., Weeber, E., Morgan, D., and Kang, D.E. (2015). Slingshot-cofilin activation mediates mitochondrial and synaptic dysfunction via Aβ ligation to β1-integrin conformers. Cell Death Differ. *22*, 1069–1070. https://doi.org/10.1038/cdd.2015.41.

45. Janelidze, S., Mattsson, N., Palmqvist, S., Smith, R., Beach, T.G., Serrano, G.E., Chai, X., Proctor, N.K., Eichenlaub, U., Zetterberg, H., et al. (2020). Plasma P-tau181 in Alzheimer's disease: relationship to other biomarkers, differential diagnosis, neuropathology and longitudinal progression to Alzheimer's dementia. Nat. Med. *26*, 379–386. https://doi.org/10.1038/s41591-020-0755-1.

46. Therriault, J., Benedet, A.L., Pascoal, T.A., Lussier, F.Z., Tissot, C., Karikari, T.K., Ashton, N.J., Chamoun, M., Bezgin, G., Mathotaarachchi, S., et al. (2021). Association of plasma P-tau181 with memory decline in non-demented adults. Brain Commun. *3*, fcab136. https://doi.org/10.1093/braincomms/fcab136.

47. Paternoster, V., Rajkumar, A.P., Nyengaard, J.R., Børglum, A.D., Grove, J., and Christensen, J.H. (2018). The importance of data structure in statistical analysis of dendritic spine morphology. J. Neurosci. Methods *296*, 93–98. https://doi.org/10.1016/j.jneumeth.2017.12.022.

48. Lazic, S.E. (2010). The problem of pseudoreplication in neuroscientific studies: is it affecting your analysis? BMC Neurosci. *11*, 5. https://doi.org/10.1186/1471-2202-11-5.

49. Braak, H., and Braak, E. (1991). Neuropathological staging of Alzheimer-related changes. Acta Neuropathol. *82*, 239–259. https://doi.org/10.1007/BF00308809.

50. Paxinos, G., and Franklin, K. (2019). The Mouse Brain in Stereotaxic Coordinates, 5th ed. (Academic Press).

51. Kim, B.G., Dai, H.N., McAtee, M., Vicini, S., and Bregman, B.S. (2007). Labeling of dendritic spines with the carbocyanine dye DiI for confocal microscopic imaging in lightly fixed cortical slices. J. Neurosci. Methods *162*, 237–243. https://doi.org/10.1016/j.jneumeth.2007.01.016.

52. Shu, L., Chen, B., Chen, B., Xu, H., Wang, G., Huang, Y., Zhao, Y., Gong, H., Jiang, M., Chen, L., et al. (2019). Brain ischemic insult induces cofilin rod formation leading to synaptic dysfunction in neurons. J. Cereb. Blood Flow Metab. *39*, 2181–2195. https://doi.org/10.1177/0271678X18785567.

53. Barker, G.R.I., and Warburton, E.C. (2011). When is the hippocampus involved in recognition memory? J. Neurosci. *31*, 10721–10731. https://doi.org/10.1523/jneurosci.6413-10.2011.

54. Barnes, C.A. (1979). Memory deficits associated with senescence: a neurophysiological and behavioral study in the rat. J. Comp. Physiol. Psychol. *93*, 74–104. https://doi.org/10.1037/h0077579.

55. Pitts, M.W. (2018). Barnes Maze procedure for spatial learning and memory in mice. Bio. Protoc. *8*, e2744. https://doi.org/10.21769/BIOPROTOC.2744.

56. Negrón-Oyarzo, I., Espinosa, N., Aguilar-Rivera, M., Fuenzalida, M., Aboitiz, F., and Fuentealba, P. (2018). Coordinated prefrontal–hippocampal activity and navigation strategy-related prefrontal firing during spatial memory formation. Proc. Natl. Acad. Sci. USA *115*, 7123–7128. https://doi.org/10.1073/pnas.1720117115.

57. Illouz, T., Madar, R., Clague, C., Griffioen, K.J., Louzoun, Y., and Okun, E. (2016). Unbiased classification of spatial strategies in the Barnes maze. Bioinformatics *32*, 3314–3320. https://doi.org/10.1093/bioinformatics/btw376.

58. Pinheiro, J., and Bates, D. (2006). Mixed-Effects Models in S and S-PLUS (Springer).

59. Bates, D., Mächler, M., Bolker, B.M., and Walker, S.C. (2015). Fitting linear mixed-effects models using lme4. J. Stat. Softw. *67*, 1–48. https://doi.org/10.18637/jss.v067.i01.

60. Kuznetsova, A., Brockhoff, P.B., and Christensen, R.H.B. (2017). lmerTest package: tests in linear mixed effects models. J. Stat. Softw. *82*, 1–26. https://doi.org/10.18637/jss.v082.i13.

61. Lenth, R. (2024). *_Emmeans: Estimated Marginal Means, aka Least-Squares Means_*. R. package version 1.10.0. https://CRAN.R-project.org/package=emmeans.